

Dynamic Ruptures on a Frictional Interface with Off-Fault Brittle Damage: Feedback Mechanisms and Effects on Slip and Near-Fault Motion

SHIQING XU,^{1,2} YEHUDA BEN-ZION,¹ JEAN-PAUL AMPUERO,³ and VLADIMIR LYAKHOVSKY⁴

Abstract—The spontaneous generation of brittle rock damage near and behind the tip of a propagating rupture can produce dynamic feedback mechanisms that modify significantly the rupture properties, seismic radiation, and generated fault zone structure. In this work, we study such feedback mechanisms for single rupture events and their consequences for earthquake physics and various possible observations. This is done through numerical simulations of in-plane dynamic ruptures on a frictional fault with bulk behavior governed by a brittle damage rheology that incorporates reduction of elastic moduli in off-fault yielding regions. The model simulations produce several features that modify key properties of the ruptures, local wave propagation, and fault zone damage. These include (1) dynamic generation of near-fault regions with lower elastic properties, (2) dynamic changes of normal stress on the fault, (3) rupture transition from crack-like to a detached pulse, (4) emergence of a rupture mode consisting of a train of pulses, (5) quasi-periodic modulation of slip rate on the fault, and (6) asymmetric near-fault ground motion with higher amplitude and longer duration on the side with reduced elastic moduli. The results can have significant implications to multiple topics ranging from rupture directivity and local amplification of seismic motion to near-fault tremor-like signals.

Key words: Mechanics of faulting, dynamic rupture, fault zone rheology, friction, fracture, brittle damage.

1. Introduction

The high stress concentration at the front of dynamic earthquake ruptures is expected to produce

brittle rock damage (reduction of elastic moduli) in the material surrounding the fault. The damage generation and associated energy absorption can reduce the amplitude of ground motion (e.g., ANDREWS *et al.*, 2007). However, the brittle damage process can contribute to the radiated wavefield (BEN-ZION and AMPUERO, 2009) and the generated damage zone with reduced elastic moduli may behave as a waveguide that can amplify near-fault motion (e.g., BEN-ZION and AKI, 1990; SPUDICH and OLSEN, 2001; AVALLONE *et al.*, 2014). Waves reflected from the boundaries of the generated damage zone may influence the subsequent rupture properties as previously shown in simulations with a pre-existing, low velocity fault zone (e.g., BEN-ZION and HUANG, 2002; HUANG and AMPUERO, 2011). Moreover, if the damage zone is asymmetrically distributed around the fault, the spontaneously generated bimaterial interface can lead to coupling between slip and dynamic change of normal stress that can change significantly the mode (pulse vs. crack) and other properties of ruptures (e.g., WEERTMAN, 1980; ANDREWS and BEN-ZION, 1997; AMPUERO and BEN-ZION, 2008).

There has been considerable research in recent years on simulations of dynamic ruptures that incorporate off-fault plastic yielding (e.g., ANDREWS, 2005; BEN-ZION and SHI, 2005; DUAN and Day, 2008; TEMPLETON and RICE, 2008; MA and ANDREWS, 2010; DUNHAM *et al.*, 2011; KANEKO and FIALKO, 2011; XU and BEN-ZION, 2013; GABRIEL *et al.*, 2013). These studies provided insights on various connections between deformation processes on and off the main faults. However, earthquake models with off-fault plasticity keep the elastic moduli in the yielding region unchanged, so they do not account for potentially important feedback mechanisms between

¹ Department of Earth Sciences, University of Southern California, Los Angeles, CA 90089-0740, USA. E-mail: stiller.xu@gmail.com; benzion@usc.edu

² Present Address: National Research Institute for Earth Science and Disaster Prevention, Tsukuba, Ibaraki 305-0006, Japan.

³ Division of Geological and Planetary Sciences, California Institute of Technology, Pasadena, CA 91125, USA. E-mail: ampuero@gps.caltech.edu

⁴ Geological Survey of Israel, Jerusalem 95501, Israel. E-mail: vladi@gsi.gov.il

generation of brittle rock damage and properties of dynamic ruptures and ground motion. Laboratory experiments (e.g., GUPTA, 1973; LOCKNER and BYERLEE, 1980; STANCHITS *et al.*, 2006) and seismological observations (e.g., PENG and BEN-ZION, 2006; WU *et al.*, 2009; FROMENT *et al.*, 2013) show that brittle failures are accompanied by significant temporal changes of elastic moduli. To study the consequences of dynamic reduction of elastic moduli near propagating ruptures, we incorporate in this work brittle off-fault damage in simulations of dynamic in-plane ruptures. Healing effects and damage evolution over multiple earthquake cycles (e.g., BEN-ZION *et al.*, 1999; LYAKHOVSKY and BEN-ZION, 2009; FINZI *et al.*, 2009) are not considered in this work.

The simulations employ a continuum visco-elastic damage model with co-evolution of inelastic strain and elastic moduli in off-fault regions where the stress reaches the elastic limit (e.g., LYAKHOVSKY *et al.*, 1997a, 2011; LYAKHOVSKY and BEN-ZION, 2008). The results illustrate the richness of new dynamical features that can arise from the interaction between ruptures on pre-existing frictional faults and dynamically evolving elastic moduli in the yielding damage zones. The spontaneous damage generation leads to local motion amplification and asymmetric near-fault ground motion behind the rupture front. We also find, under some conditions, transitions of the rupture mode to different types of pulses and oscillatory slip rate that may produce tremor-like signals near the fault.

2. Model Description

We consider 2-D in-plane ruptures and off-fault brittle damage allowing dynamic changes of elastic moduli under plane strain conditions. The relevant stress components operating on the fault and the surrounding medium are listed in Fig. 1. A right-lateral rupture is nucleated with a prescribed speed over a small patch (red portion in Fig. 1) until it can propagate spontaneously along the frictional fault (solid black line in the center). The first motion of P-waves radiated from the hypocenter defines four quadrants, with “C” and “T” denoting

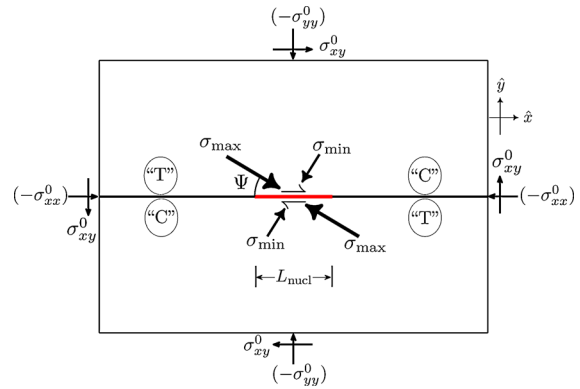


Figure 1

Model configuration for dynamic ruptures along a frictional interface (black line at the center) with possible generation of brittle damage in the surrounding bulk. The rupture is nucleated right-laterally with a prescribed speed over a small patch (red portion) until it can propagate spontaneously. The angle Ψ characterizes the relative orientation of the background maximum compressive stress to the fault. Symbols “C” and “T” denote the compressional and extensional quadrants, respectively, in relation to the first motion of P-waves radiated from the nucleation zone. Because of the 180° rotational symmetry with respect to the hypocenter, only the right half will be shown in later plots; all the simulated features (e.g. signs of stress changes, rupture properties) to the right also hold for the left direction

compressional and extensional quadrants, respectively. The initial normal and shear stresses on the fault are $\sigma_0 = \sigma_{yy}^0$ and $\tau_0 = \sigma_{xy}^0$, respectively, and Ψ represents the angle between the maximum background compressive stress σ_{max} and the fault. A relative strength parameter $S = (\tau_s - \tau_0)/(\tau_0 - \tau_d)$ is used to quantify the relation between initial shear stress, static strength $\tau_s = f_s(-\sigma_0)$ and dynamic strength $\tau_d = f_d(-\sigma_0)$, with f_s and f_d being the static and dynamic friction coefficient, respectively. It is known that increasing the initial shear stress level towards the static strength can induce a transition to supershear ruptures (BURRIDGE, 1973; ANDREWS, 1976; DAS and AKI, 1977; DAY, 1982). In this study, we choose the value of S and rupture propagation distance range to produce subshear ruptures relative to the shear wave speed of the intact medium. We will later discuss the relation between rupture speed and the wave speed of the spontaneously generated damaged material.

2.1. Nucleation Procedure, Friction Law, and Normal Stress Regularization

We follow the procedure of XU *et al.* (2012a) with a time-weakening friction (TWF) to trigger artificially the rupture within the nucleation zone. The rupture front during the nucleation stage is enforced to propagate outward with a constant subshear speed. The frictional strength at locations reached by the prescribed rupture front linearly weakens with time up to the dynamic level τ_d . An associated length scale R^{TWF} can be defined over which the fault strength spatially reduces from τ_s to τ_d , and is well resolved by the employed numerical cells. The actual time duration of the prescribed nucleation process is limited by the onset of spontaneous rupture propagation under a friction law that is described below.

We adopt a linear slip-weakening friction (SWF) to describe physically the breakdown process along the fault outside the nucleation zone. Specifically, the frictional strength τ and the normal stress σ are related by $\tau = f(-\sigma)$ where the friction coefficient f has the following dependence (e.g., IDA, 1972; PALMER and RICE, 1973; ANDREWS, 1976) on slip Δu :

$$f = \begin{cases} f_s - (f_s - f_d)\Delta u/D_c & \text{if } \Delta u \leq D_c \\ f_d & \text{if } \Delta u > D_c \end{cases}, \quad (1)$$

where D_c is a characteristic slip distance over which the friction coefficient reduces from f_s to f_d . We define the static and dynamic fault strength as τ_s and τ_d , respectively. When the background shear stress is only slightly higher than τ_d , the size of the spatial region associated with the strength reduction, referred to as the process zone, can be estimated (e.g., RICE, 1980) by

$$R = \frac{R_0}{f_{\text{II}}(v_r)}, \quad (2a)$$

where $f_{\text{II}}(v_r)$ is a monotonic function of rupture speed v_r that increases from unity at $v_r = 0$ to infinity at the limiting Rayleigh wave speed, and R_0 is the static value of R at zero rupture speed assuming the normal stress is equal to its initial value. For Poissonian solids, this is given by

$$R_0 = \frac{3\pi}{8} \frac{\mu D_c}{(\tau_s - \tau_d)}, \quad (2b)$$

where μ is the shear modulus. To provide proper numerical resolution for the simulations with evolving elastic rock properties, we discretize R_0 (by using the μ value of intact rocks) with multiple numerical cells. We numerically measure the dynamic value of R during rupture propagation (from snapshots of along-fault quantities) to ensure that the process zone is always well resolved.

A related consideration for this study is the fault frictional response under abrupt changes of normal stress, owing to the possible damage-related material contrast across the fault. To ensure the numerical stability in such scenarios, a Prakash-Clifton normal stress regularization of the type proposed by RUBIN and AMPUERO (2007) is adopted. We assume that the frictional strength is proportional to a modified normal stress σ^* whose evolution is described by:

$$\dot{\sigma}^* = \frac{|V| + V^*}{\delta_c} (\sigma - \sigma^*), \quad (3)$$

where V^* and δ_c are characteristic slip rate and slip distance, respectively, and V is the slip rate. Similar to XU *et al.* (2012a), we choose the values for V^* and δ_c so that normal stress regularization is only moderately, but not overly emphasized. A discussion on the influence of wave-induced normal stress changes at a spontaneously generated local bimaterial interface behind the rupture front is given in Appendix.

2.2. Brittle Damage Rheology for the Bulk

We follow the model formulation of LYAKHOVSKY *et al.* (2011) and related works (e.g., LYAKHOVSKY *et al.*, 1997a, b; HAMEL *et al.*, 2004; BEN-ZION and LYAKHOVSKY, 2006; LYAKHOVSKY and BEN-ZION, 2008) to describe the material response under brittle deformation. The elastic potential energy per unit mass accounting for internal damage is expressed as:

$$U(\varepsilon_{ij}^e, \alpha) = \frac{1}{\rho} \left(\frac{\lambda}{2} I_1^2 + \mu I_2 - \gamma I_1 \sqrt{I_2} \right) \quad (4)$$

where ρ is the mass density, λ and μ are the Lamé parameters, $I_1 = e_{kk}^e$ and $I_2 = e_{ij}^e e_{ij}^e$ are the first and second strain invariants. A more general expression may depend also the third strain invariant. However, LYAKHOVSKY *et al.* (1997b) and others demonstrated

that the dependency of the elastic potential for rocks on the third strain invariant, I_3 , is very weak and can be neglected. The parameter γ is an additional modulus responsible for the coupling between volumetric and shear strain. This modulus vanishes in a damage-free solid. The elastic strain tensors ε_{ij}^e and a damage scalar α are treated as state variables, with α interpreted as a non-dimensional measure of microcrack density in a macroscopically representative volume (LYAKHOVSKY *et al.*, 1997a). In the field, α may be estimated from comparisons of measured elastic moduli with reference values of intact rocks of the same type and models such as BUDIANSKY and O'CONNELL (1976), while in our study it is scaled to have a simple explicit connection to elastic moduli. The elastic moduli in Eq. (4) are assumed to have the following dependence on the damage variable α :

$$\begin{aligned}\lambda &= \lambda_0 \\ \mu &= \mu_0 + \xi_0 \gamma_r \alpha \\ \gamma &= \gamma_r \alpha\end{aligned}\quad (5)$$

where λ_0 and μ_0 are the Lamé parameters of the intact solid, ξ_0 is a material parameter (with a negative value) related to the onset of damage generation, and γ_r is a scaling factor that maps damage into elastic moduli and sets the maximum damage level at one. The parameter ξ_0 can be connected to the internal friction angle ϕ :

$$\xi_0 = \frac{-\sqrt{2}}{\sqrt{1 + (\lambda_0/\mu_0 + 1)^2 \sin^2 \phi}}. \quad (6)$$

Equation (6) is the 2-D version of the relation derived by LYAKHOVSKY *et al.* (1997a). From the above expressions, a non-linear stress-strain relation can be readily derived as

$$\sigma_{ij} = \rho \frac{\partial U}{\partial \varepsilon_{ij}^e} = (\lambda I_1 - \gamma \sqrt{I_2}) \delta_{ij} + (2\mu - \gamma I_1 / \sqrt{I_2}) \varepsilon_{ij}^e. \quad (7)$$

For deformations with non-zero I_1 , the above equation may be re-written using effective moduli depending on $\xi = I_1 / \sqrt{I_2}$:

$$\sigma_{ij} = (\lambda - \gamma/\xi) I_1 \delta_{ij} + (2\mu - \gamma \xi) \varepsilon_{ij}^e. \quad (8)$$

Depending on the level of internal damage, the elastic potential energy U may lose its convexity

under different types of loading (see LYAKHOVSKY *et al.*, 1997a, 2011, for a detailed discussion on this topic). Mathematically, the loss of convexity leads to non-uniqueness of the solutions to quasi-static problems, while physically it signifies brittle instability and change in the state of the material (e.g., LYAKHOVSKY and BEN-ZION, 2014a, b). From a computational perspective, a loss of convexity of the energy function can lead to severe numerical instabilities, and thus needs to be carefully regularized.

The energy function U is convex if all the eigenvalues of the Hessian matrix ($\partial^2 U / \partial \varepsilon_{ij}^e \partial \varepsilon_{kl}^e$) are positive (see Table 1; note that $\varepsilon_{13}^e = \varepsilon_{23}^e = \varepsilon_{33}^e = 0$ for the adopted plane strain conditions, and all terms were multiplied by the density to get the pressure units). The first and second eigenvalues can be calculated as the roots of a quadratic equation

$$x^2 + bx + c = 0, \quad (9)$$

which is associated with the 2×2 sub-matrix in the upper left of Table 1:

$$\begin{aligned}b &= -(2\lambda + 4\mu - 3\gamma\xi), \\ c &= (2\mu - \gamma\xi)^2 + (2\mu - \gamma\xi)(2\lambda - \gamma\xi) + (\lambda\gamma\xi - \gamma^2)(2 - \xi^2).\end{aligned}\quad (10)$$

With the above expressions, the corresponding conditions for the loss of convexity are:

$$\begin{aligned}A_1 &= (-b - \sqrt{b^2 - 4c})/2 = 0, \\ A_2 &= (-b + \sqrt{b^2 - 4c})/2 = 0.\end{aligned}\quad (11)$$

The third eigenvalue is given by the isolated principal minor in the lower right of Table 1, and the corresponding condition for the loss of convexity is:

$$A_3 = 2\mu - \gamma\xi = 0. \quad (12)$$

Each condition in Eqs. (11) and (12) defines a characteristic curve in the $\xi - \alpha$ phase space, which can be used to distinguish materials in different regimes. Figure 2 shows such a phase diagram within the range of the current 2-D study ($-\sqrt{2} \leq \xi \leq \sqrt{2}$, $0 \leq \alpha \leq 1$). Equations (11) and (12) normalized by μ_0 are plotted with different colors to separate material phases with or without losing convexity of different types, and the superposed black curve defines the combined boundary for all the

Table 1

Hessian matrix of U (multiplied by ρ) $\rho(\partial^2 U / \partial e_{ij}^e \partial e_{kl}^e)$ in 2-D

	e_{11}^e	e_{22}^e	e_{12}^e
e_{11}^e	$\lambda + 2\mu - \gamma\xi + \gamma\xi e_1^2 - 2\gamma e_1$	$\lambda - \gamma(e_1 + e_2) + \gamma\xi e_1 e_2$	0
e_{22}^e	$\lambda - \gamma(e_1 + e_2) + \gamma\xi e_1 e_2$	$\lambda + 2\mu - \gamma\xi + \gamma\xi e_2^2 - 2\gamma e_2$	0
e_{12}^e	0	0	$2\mu - \gamma\xi$
Notation	$e_1 = e_{11}^e / \sqrt{I_2}$, $e_2 = e_{22}^e / \sqrt{I_2}$, where e_1^e and e_2^e are principal strains		

The original 3-D version can be found in Table 1 of LYAKHOVSKY *et al.* (1997a)

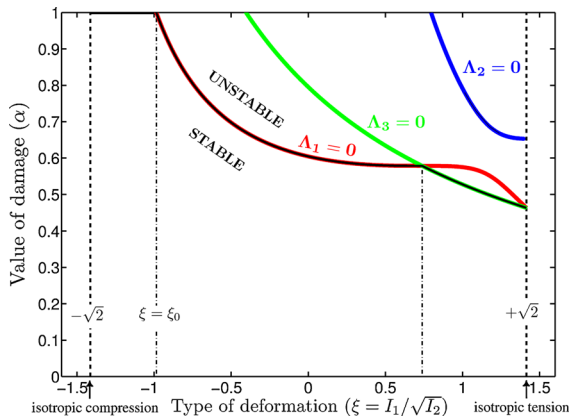


Figure 2

A $\xi - \alpha$ phase diagram characterizing rock behaviors in different deformation regimes as a function of internal damage in 2-D. From left to right $\xi = -\sqrt{2}$ and $\xi = \sqrt{2}$ correspond to isotropic compaction and tension, respectively, while the deformation has non-zero shear component in between. The threshold value ξ_0 defines the level of ξ above which damage starts to accumulate. From bottom to top $\alpha = 0$ corresponds to purely elastic solid without internal damage, while $\alpha = 1$ defines the maximum damage level where convexity is lost at ξ_0 . Red and blue curves correspond to the conditions with loss of convexity in Eq. (11), and the green curve corresponds to the condition defined in Eq. (12); all the conditions are normalized by μ_0 . The piece-wise black curve defines the common boundary between preserving and losing convexity for all possibilities. A corresponding 3-D version can be found in Fig. 1 of LYAKHOVSKY *et al.* (1997a)

possibilities. We note that $A_1 = 0$ is the strongest condition in the compressive ($\xi < 0$) or slightly tensile ($\xi > 0$) regime, while $A_3 = 0$ dominates in the vicinity of 2-D extension ($\xi \rightarrow \sqrt{2}$). For our focus on earthquake-related deformation, we mainly use $A_1 = 0$ to discuss the issue of convexity.

During damage accumulation, the modulus γ increases and the shear modulus μ decreases. This leads to material evolution from linear elastic solid ($\alpha = 0$) to macroscopic brittle instability at a critical damage level (α_{cr}) leading to loss of convexity.

LYAKHOVSKY *et al.* (1997a, 2011) derived an evolution equation for the damage state variable using energy and entropy balance equations and requiring non-negative entropy production. Previous studies with the damage model have shown that constant remote loading leads to an accelerated damage accumulation once exceeding the threshold ξ_0 for damage onset (e.g., BEN-ZION and LYAKHOVSKY, 2002). This would produce inevitable loss of convexity unless the local stress is relaxed rapidly. To regularize the damage evolution close to the critical state leading to loss of convexity, we simplify the model developments of LYAKHOVSKY *et al.* (2011) by adding a damping term that becomes effective when the critical state is approached. The resulting equation for damage evolution is

$$\dot{\alpha} = \begin{cases} I_2 \left[C_d (\xi - \xi_0) - \frac{q}{A^2} \right] & \text{if } \xi \geq \xi_0 \\ 0 & \text{if } \xi < \xi_0 \end{cases} \quad (13)$$

where C_d is a model parameter controlling the rate of damage growth, the q -term is added to damp the damage growth near the critical state $A = \min(A_1, A_3) / \mu_0 \rightarrow 0$. Note that eigenvalues in Eqs. (11) and (12) physically have a unit of elastic modulus. To facilitate the understanding of A , we normalize its value by μ_0 in the numerical implementation, such that its distribution in terms of a non-dimensional contour map can be easily shown in the $\xi - \alpha$ phase space (Fig. 3). This map quantifies the closeness of the material element to the critical state in the $\xi - \alpha$ phase space.

Following the interpretation of LYAKHOVSKY *et al.* (2011) and LYAKHOVSKY and BEN-ZION (2014a, b), $A = 0$ separates between solid-like ($A > 0$) and granular-like ($A < 0$) states of material in the compressive and partially tensile regime. This is illustrated in Fig. 3 with a gradual phase transition

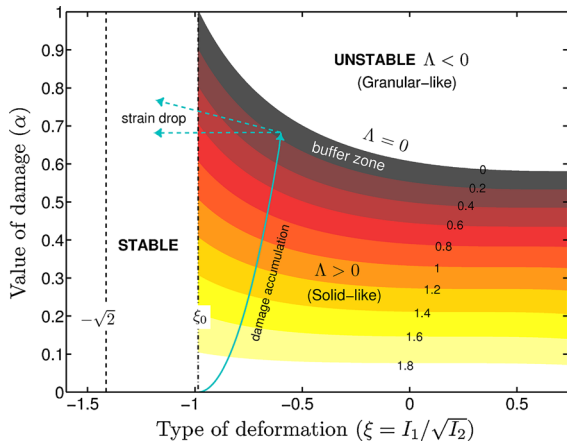


Figure 3

A schematic diagram showing the path of damage evolution in $\xi - \alpha$ phase space, where the condition $A_1 = 0$ dominates the determination of loss of convexity (red curve in Fig. 2). The background color shows the normalized contour map (divided by μ_0) of A_1 (here, simplified as A) as a function of ξ and α . Damage starts to accumulate once $\xi \geq \xi_0$, but is damped by a “buffer zone” (the grey belt region) near the critical state ($A = 0$), where a granular-related plasticity can significantly relax the strain. With a fixed value of C_d , the width of the buffer zone will be predominantly controlled by the damping parameter q in Eq. (13), and the phase-transition parameter β in Eq. (14)

between solid-like and granular-like phases of a material under brittle deformation. The dependence of the transition state on a mechanical variable (ξ) and an entropy-related variable (α) is analogous to the pressure–temperature diagrams of classical phase transitions. A probability function describing how solid-like a material element is may be defined as

$$P(A) = \frac{1}{\exp(-A/\beta) + 1}, \quad (14)$$

where β is a parameter quantifying the width of the phase transition zone between solid-like and granular-like states. Two end-member cases relevant for this model formulation are $P\left(\frac{A}{\beta} \gg 1\right) \rightarrow 1$ for solid-like phase far away from the transition level and $P\left(\frac{A}{\beta} \rightarrow 0\right) \rightarrow 1/2$ when the transition state is approached.

Two separate terms can contribute to the accumulation of plastic strain during failure (LYAKHOVSKY *et al.*, 2011):

$$\dot{\epsilon}_{ij}^p = [C_g(1 - P) + C_v\dot{\alpha}] \tau_{ij}. \quad (15)$$

The first term arises from the intrinsic viscous behavior of the granular phase, which scales with the

probability of the granular state $1 - P$ (LYAKHOVSKY *et al.*, 2011). The second term was originally proposed by HAMIEL *et al.* (2004) and represents the ordinary generation of damage-induced plastic deformation. Similar to previous studies, we assume that plastic strain is partitioned to different components according to the deviatoric stress $\tau_{ij} = \sigma_{ij} - 1/2\sigma_{kk}\delta_{ij}$ (in 2-D).

2.3. Numerical Method and Model Parameterization

The simulations are performed using a 2-D spectral element code (AMPUERO, 2002; SEM2D-PACK-2.3.8, 2012, available at <http://sourceforge.net/projects/sem2d/>), with implementation of the presented brittle damage rheology. We extended the initial work by AMPUERO *et al.* (2008) to incorporate the control on loss of convexity (Eqs. 13–15). Absorbing boundary conditions are assumed around the calculation domain, which is set large enough to ensure no interference with the propagating rupture and the generated off-fault damage. A visco-elastic layer of the Kelvin–Voigt type is added surrounding the fault to damp the high-frequency numerical noise. The implementation of a non-linear bulk rheology is described by LYAKHOVSKY *et al.* (2009). The accuracy of this code has been validated by various studies (AMPUERO, 2002; HUANG and AMPUERO, 2011; GABRIEL *et al.*, 2013; XU *et al.*, 2012a; see also the user’s guide of SEM2DPACK-2.3.8, 2012).

Similar to our previous studies with off-fault plasticity (XU *et al.*, 2012a, b), the calculated quantities are normalized by reference parameters. Table 2 lists values of basic parameters that are fixed unless mentioned otherwise. We set the static friction coefficient at 0.6, within the range of typical values measured by laboratory experiments (LOCKNER and BEELER, 2002). For most of the studied cases we set the dynamic friction coefficient at 0.1, as found in frictional experiments under high slip rate (DI TORO *et al.*, 2011). Table 3 summarizes the conversion between the physical and normalized quantities that are frequently discussed in this study. We typically use in the simulations an average grid size (average spectral node spacing) of $\bar{\Delta}x \approx L_0/4$ with L_0 as a reference unit length scale (see Table 2), which is equivalent for most assumed stress and friction

Table 2

Model parameters and reference values

Parameters	Value
Lamé parameters for intact rocks λ_0, μ_0	1, 1
<i>P</i> - and <i>S</i> -wave speeds for intact rocks c_p^0, c_s^0	1.732, 1
Mass density ρ	1
Reference unit length scale L_0	1
Characteristic length scale (TWF) R^{TWF}	$4L_0$
Characteristic slip distance (SWF) D_c	$2L_0$ or $5.6L_0$
Static friction coefficient f_s	0.6
Dynamic friction coefficient f_d	Variable
Static size of process zone (SWF) R_0	Variable
Critical elastic strain invariant for the onset of rock damage ξ_0	-0.98

Table 3

Conversion between physical and normalized quantities

Length	Time	Slip rate	Normal stress change	Shear stress change
$l' = \frac{l}{R_0}$	$t' = \frac{tc_s^0}{R_0}$	$\Delta u' = \frac{\Delta u R_0}{D_c c_s^0}$	$\Delta \sigma' = \frac{\Delta \sigma}{ \sigma_0 }$	$\Delta \tau' = \frac{\Delta \tau}{(\tau_0 - \tau_d)}$

coefficient values to $\overline{\Delta x} \approx R_0/53$. We note that the physical length scale R_0 is fixed in each case, but may change among cases since it depends on the initial normal stress, friction coefficients, and D_c values (Eq. 2b), while the reference length scale L_0 is the same for all cases. For convenience we present length scales in the simulated results in terms of both R_0 and L_0 . For cases requiring very large domains, we switch to a doubled grid size, but check that the key features are not influenced.

3. Results

In principle, we could perform a detailed parameter-space study to investigate how different model parameters can influence properties of the generated damage zones and their interaction with fault motion. However, since the adopted damage model shares some similarities with plasticity, such as the dependence of the location and extent of damage zones on the background stress and rupture mode (AMPUERO *et al.*, 2008), we mainly present additional features that are produced with the damage model and can be relevant to the interpretation of various observations.

3.1. Dynamic Changes of Normal Stress on the Fault

One important feature produced by off-fault brittle damage is coupling between slip and dynamic changes of the normal stress $\Delta\sigma$ on the fault, induced by the bimaterial effect. It is well known that during propagation of mode-II ruptures in a linear homogeneous elastic medium, the normal stress does not change on the fault because of the symmetry in the fault-normal displacement field. However, a contrast of elastic properties across the fault breaks the symmetry and leads to coupling between $\Delta\sigma$ and slip. For a bimaterial frictional fault, the sign and amplitude of $\Delta\sigma$ depend on the sense of slip, degree of material contrast, rupture propagation direction, position relative to the rupture front, and rupture speed regime (e.g., WEERTMAN, 1980, 2002; BEN-ZION, 2001). Here, we show that the expected changes of normal stress can also be observed with the spontaneous generation of a material contrast across the fault, owing to an asymmetric pattern of damage generation (through Eqs. 5, 13). We note that the non-linear stress-strain relation for a damaged medium (Eqs. 7, 8) may also contribute to $\Delta\sigma$ even under a pure shear deformation ($I_1 = 0$).

Figure 4a, b show the spatial distributions, at a selected time, of the effective shear wave speed calculated by $\sqrt{\mu(\alpha)/\rho}$ for cases with background stress orientations $\Psi = 14^\circ$ and 56° , respectively. A more accurate calculation of the shear wave speed in the damaged material would also take into consideration the stress level, and account for stress- and damage-induced anisotropy (HAMIEL *et al.*, 2009), but for simplicity this is not done here. The low and high Ψ values are chosen as representative of thrust and large strike-slip faults, respectively. The Ψ values were shown to be important for determining the location of dynamically generated off-fault yielding (e.g., TEMPLETON and RICE, 2008; AMPUERO, *et al.*, 2008; XU *et al.*, 2012a, b). The inset grey plots in Fig. 4 show strain-based predictions of the current failure zone based on Eqs. 6 and 13. We use such predictions to constrain the selected values for C_d and q (Eq. 13), so that the damage zone can be generated dynamically without too much delay in response to high ξ value. The stress-based theoretical analysis of XU

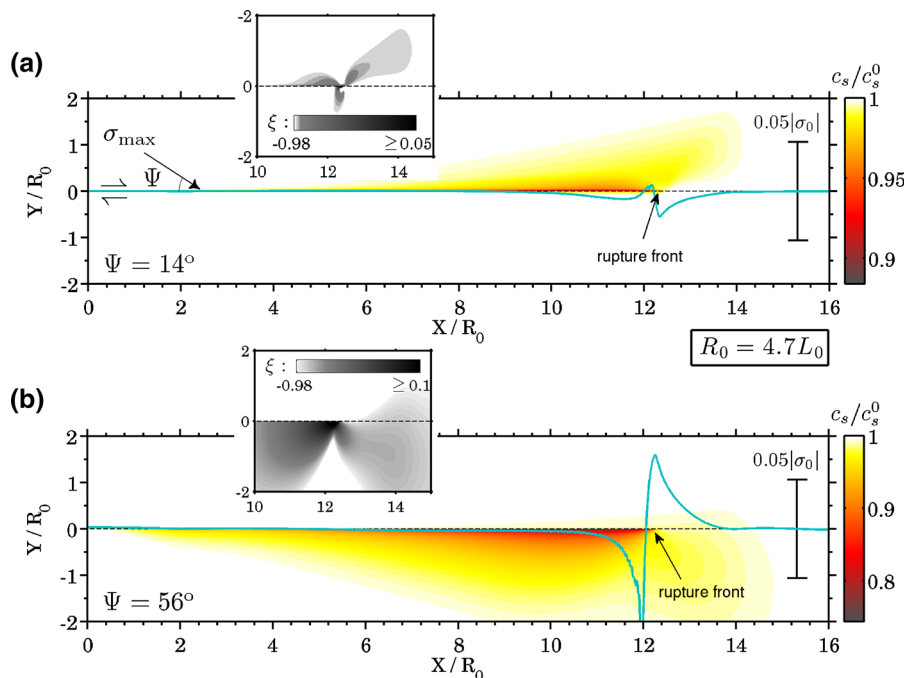


Figure 4

Snapshot distributions of the mapped shear wave speed (based on the evolving damage) for cases with (a) $\Psi = 14^\circ$ and (b) $\Psi = 56^\circ$. For both plots, $D_c = 2L_0$ (it is set at $5.6L_0$ for all other cases), $C_d = 0.25c_s^0/L_0 \approx 1.2c_s^0/R_0$, $C_v = 1/\mu_0$, and $C_g = 0$. Normal stress change $\Delta\sigma$ along the fault is imposed in each plot, with a reference *scale bar* on the right. Positive and negative values indicate tensile and compressive changes, respectively. The *inset grey plots* show the current failure zone defined by $\xi \geq \xi_0$ at the same time. As an illustration for the basic roles of damage, granular-related damping is turned off ($q = 0$) and results are shown only for a limited rupture propagation distance

and BEN-ZION (2013) could also explain well the generated yielding zones.

As seen by the curves in Fig. 4, there is a tensile normal stress change right behind the rupture front for $\Psi = 14^\circ$ with reduced shear wave speed mainly on the compressional side, and a compressive normal stress change in the corresponding location for $\Psi = 56^\circ$ with reduced shear wave speed on the extensional side. These normal stress changes and their dependence on the location of off-fault damage (compliant) zone are generally consistent with results associated with a pre-existing material contrast across the fault (e.g., ANDREWS and BEN-ZION, 1997; BEN-ZION and ANDREWS, 1998; SHI and BEN-ZION, 2006). On the other hand, the amplitude of the normal stress change may be modified by plasticity-related stress relaxation (DUAN, 2008b; DeDONTNEY *et al.*, 2011), as well as details of the regularization of normal stress changes (RUBIN and AMPUERO, 2007; AMPUERO and BEN-ZION, 2008).

3.2. Development of a Detached Pulse Front

According to the basic results in Sect. 3.1, there is a compressive normal stress change behind the rupture front for $\Psi = 56^\circ$. If this is the only feedback mechanism produced by off-fault brittle damage, the dynamic strength drop would be reduced and the propagating rupture would be somewhat suppressed compared to cases with zero or tensile normal stress change. In other words, this is the most unfavorable direction for rupture propagation on a bimaterial interface. Moreover, the rupture (if sustained) would generally remain crack-like with the adopted nucleation approach and friction law (DUAN, 2008b). On the other hand, the generated damage zone is expected to modify the rupture properties through interactions between waves reflected from the boundaries of the damage zone and the propagating rupture (e.g., HARRIS and DAY, 1997; BEN-ZION and HUANG, 2002; HUANG *et al.*, 2014). However, in contrast to

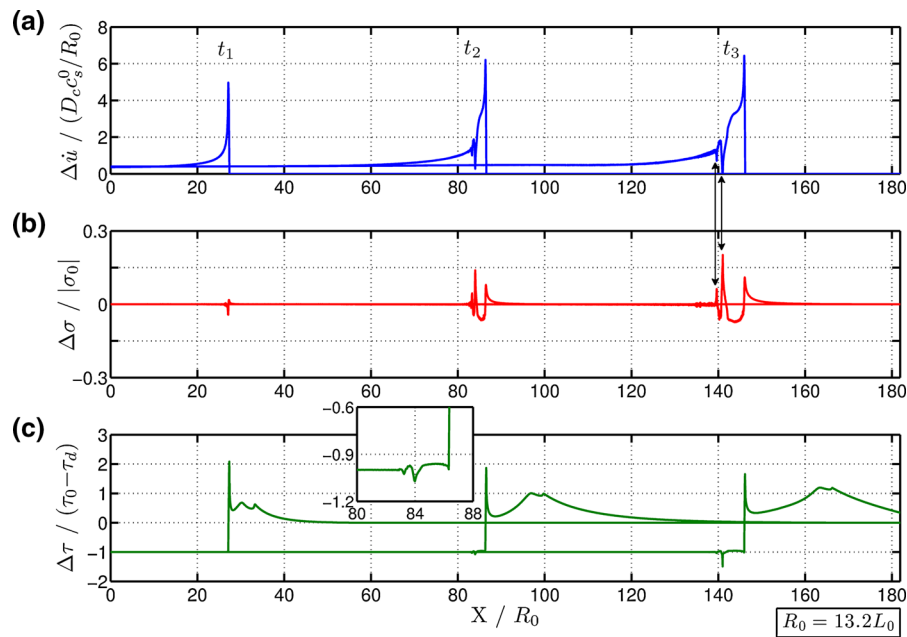


Figure 5

Spatial distributions of (a) slip rate, (b) normal stress change, and (c) shear stress change for a case with $\Psi = 30^\circ$ at three time steps. The simulation employs $f_d = 0.1$, $C_d = 0.1c_s^0/L_0 \approx 1.32c_s^0/R_0$, $q \approx 0.66c_s^0/R_0$, $C_g \approx 0.53c_s^0/(\mu_0 R_0)$, $C_v = 0$, and $\beta = 0.2$. The chosen times highlight the moments when the propagating rupture behaves like a crack (t_1), with a partially (t_2) or completely (t_3) detached pulse front. The black arrows connecting (a) and (b) at time t_3 indicate two notable tensile $\Delta\sigma$ regimes behind the rupture front, both of which are associated with a local reduction in slip rate

previous studies of bimaterial ruptures with a low velocity zone (LVZ), the damage zone bounding the fault here is evolving, leading to more complex responses. Below we discuss a case where a detached pulse is produced by the interactions between the rupture and asymmetrically generated off-fault damage zone.

Figure 5 shows the slip rate (panel a), normal stress change (panel b) and shear stress change (panel c) for a simulation similar to that producing Fig. 4b, but with $\Psi = 30^\circ$ and much longer propagation distance. At the early stage, the slip rate profile still displays a classic crack style (time t_1). However, with increasing rupture propagation distance and damage generation, there are additional tensile changes of normal stress and shear stress reduction further behind the rupture front. The net effect leads to a local reduction of slip rate at time t_2 and finally produces a completely detached pulse front at time t_3 . When a detached pulse front has formed, there is a sharp shear stress trough (lower than the frictional strength despite a tensile normal stress change) in the

region between the pulse front and the remaining slipping patch (Fig. 5c, at time t_3), which resembles what is observed in elastic homogeneous calculations with a triggered supershear pulse front (Fig. 1b of FESTA and VILOTTE, 2006). Since there is no rate-dependent healing in the employed friction law, the detached pulse front is followed by a long tail of freely slipping patch under dynamic friction, where a second pulse may be further developed (see the left arrow between Fig. 5a, b). However, if we allow a rapid healing on the frictional fault once the slip rate is below a certain threshold value (as in HUANG and AMPUERO, 2011), a pure pulse-type rupture could be generated after the transition.

Next we investigate and discuss details of the transition process to the detached pulse front. As mentioned, reflected waves within the LVZ are most likely responsible for producing the slip arrest. To confirm this expectation in the context of spontaneously evolving LVZ, we first plot the damage distribution and its off-fault variation in Fig. 6. As seen, within the overall damage zone, there is an

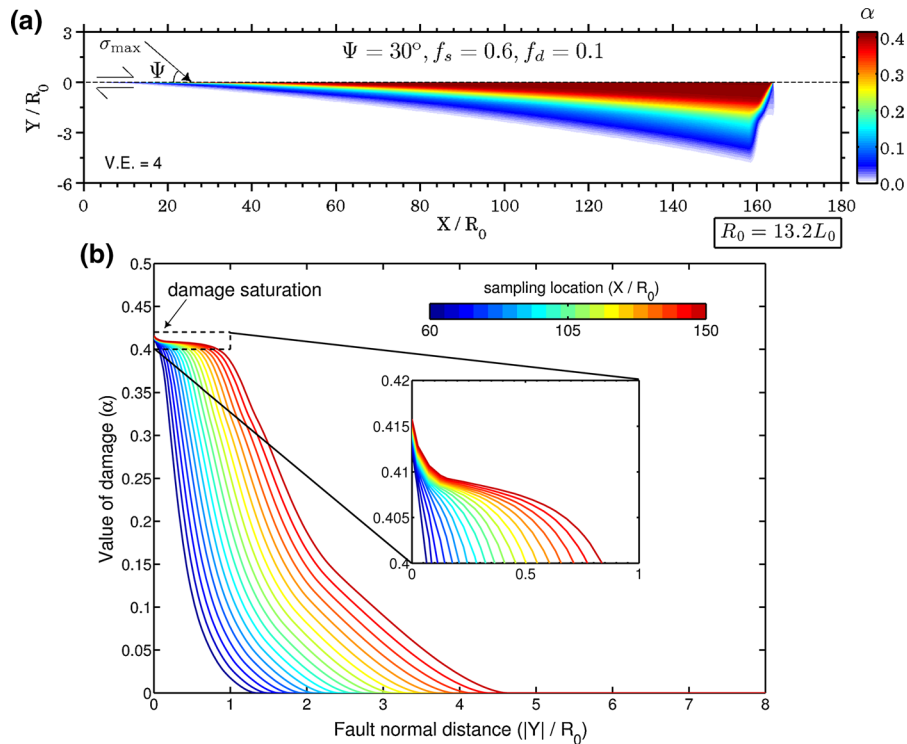


Figure 6

Snapshot distributions of (a) damage and (b) its off-fault variation for the case of Fig. 5. The color bar in (b) indicates how the sampling locations (on the extensional side) are mapped to different colors: from $X = 60R_0$ (blue) to $X = 150R_0$ (red). Note the asymptotic saturation of damage with proximity towards the fault, where a narrow waveguide within the overall LVZ may be defined

internal region near the fault that contains a high damage level with relatively gradual spatial variation. This internal region acts as an effective waveguide and provides the key structural element for generation of reflected waves rather than the overall damage zone, although both have growing width with increasing rupture length. The generated configuration is similar to the two-fault-zone-layers model of BEN-ZION (1998), with a narrow internal layer of significant velocity reduction that is responsible for key properties of the generated trapped waves, and adjacent transition zone that adds complexities to the wavefield.

Figure 7 displays zoom-in views of the mapped effective shear wave speed, the associated fault-normal particle velocity \dot{u}_y , and normal stress change $\Delta\sigma_{yy}$ near the rupture front. As clearly shown in Fig. 7c, there are series of alternating normal stress changes behind the rupture front, generally with opposite signs on different sides of the fault. The position of the first tensile normal stress change

regime behind the rupture front (on the fault and to the compressional side) more or less coincides with the location where a fresh wedge-shape LVZ has just formed (Fig. 7a). The precise boundary where waves are reflected to heal the rupture is difficult to discern from the current particle velocity distribution (Fig. 7b), because of the complex geometry of the LVZ near the rupture front and its evolving shape. For comparison, Figs. 8 and 9 show corresponding results generating single or multiple detached pulse front(s) and alternating normal stress changes (Fig. 9) behind the rupture front in elastic calculations with a pre-existing asymmetric finite-width LVZ. The similarity between those results and the (somewhat more complex) fields shown in Fig. 7 with evolving off-fault damage suggests that wave reflection contributes to the rupture healing process. In particular, the localized negative slip rate observed at some time steps in Figs. 8 and 9 implies that the sign of absolute shear stress can be temporarily reversed by reflected waves. This turns out to be the dominant factor that

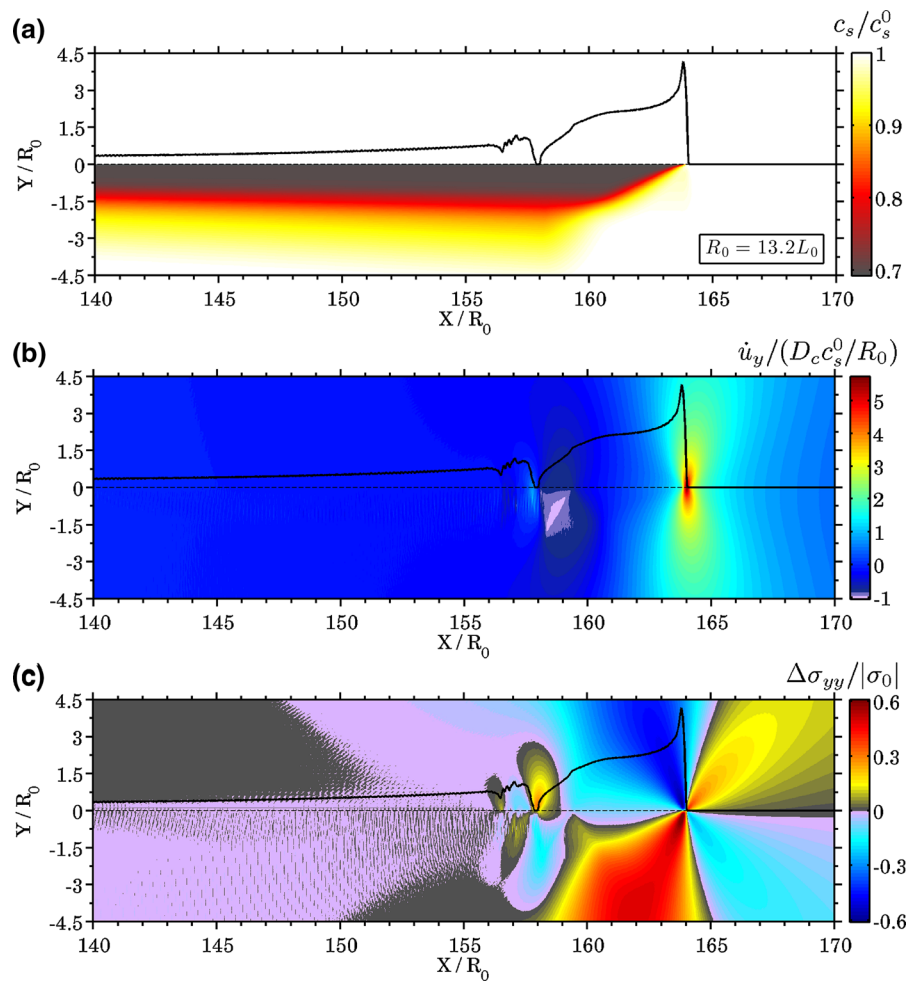


Figure 7

Snapshot distributions in a zoom-in view of (a) mapped shear wave speed, (b) fault-normal particle velocity \dot{u}_y , and (c) normal stress change $\Delta\sigma_{yy}$ for the case of Fig. 6. The distribution of slip rate at the same time is superimposed in each plot

produces the healing signal regardless of a tensile normal stress change at the same location. The operating mechanism may also include the contribution of head waves (e.g., BEN-ZION, 1989, 1990; HUANG *et al.*, 2014) that are backward-propagating along the boundaries of the LVZ, and an asymmetric “Mach front” only on the extensional side with a speed faster than the shear wave speed of the LVZ $\sim 0.7(c_s^0)$ that remains behind (Fig. 10). These mechanisms are expected because there are linear features in the particle velocity distribution (Fig. 7b) around $X = 159R_0$, which are usually observed for head waves or a Mach front (as well as its reflected counterpart within an LVZ).

In addition to the complex wave signals around the rupture front, waves are also emitted from the tail of the detached pulse front and propagate backward (Fig. 7b, c). Some of these waves become internally reflected or trapped inside the well-established LVZ further behind the rupture front. When such waves reach the fault, they may result in oscillations of slip rate in the freely slipping patch of the fault, similar to what have been illustrated in the results and Appendix of BEN-ZION and Huang (2002) for the interaction with the rupture front; see also HUANG and AMPUERO (2011) and Huang *et al.* (2014). The generation of trapped-type waves is enhanced by the following two conditions that exist further behind the rupture front:

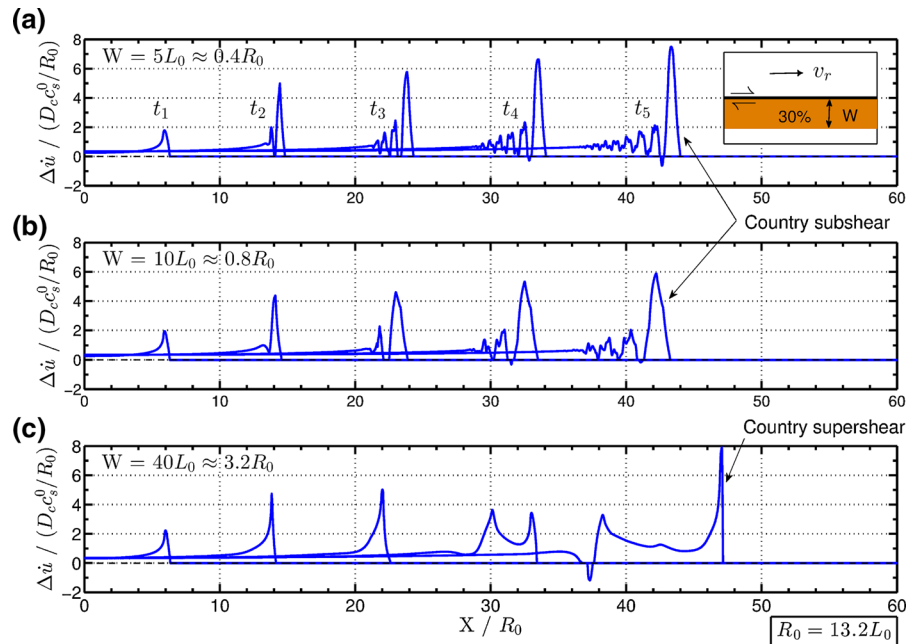


Figure 8

Snapshot distributions of slip rates for elastic calculations with a pre-existing finite-width (W) LVZ (see *inset* in **a**). **a** $W = 5L_0 \approx 0.4R_0$, **b** $W = 10L_0 \approx 0.8R_0$ and **c** $W = 40L_0 \approx 3.2R_0$. For all cases, the P- and S-wave speeds have a 30% reduction inside the LVZ compared to those of the country rocks

(1) a well-established LVZ with minor additional shape evolution to allow constructive interference of internal wave reflections, and (2) smooth distribution of background particle velocity with a relatively low amplitude. The effects of these trapped waves on rupture dynamics and near-fault ground motion are discussed in subsequent subsections.

3.3. Development of Slip Rate Oscillations

Since internal wave reflections can provide an additional feedback mechanism between off-fault brittle damage and rupture dynamics, we may use analytical and numerical model results with a pre-existing LVZ (e.g., BEN-ZION, 1998; HUANG *et al.*, 2014) to investigate the influence of different mechanisms (velocity contrast inside and outside the damage zone, rupture propagation distance, width of the damage zone, damping effects) on the efficiency of generating internal wave reflection and its interaction with the propagating rupture. Here, we mainly focus on one feature generated by our numerical simulations, the development of slip rate oscillations under certain conditions.

Figure 11 shows snapshots of slip rate (a), normal stress change (b), and shear stress change (c) for a case with $\Psi = 30^\circ$ and slightly different values of other model parameters (see caption) from those leading to Fig. 5, generating a narrower damage zone. Similar to the results in Fig. 5, the rupture initially behaves as a crack (time t_1), and later has an abrupt reduction in slip rate behind the rupture front (time t_2). In contrast to the previous results, however, at a later stage (time t_3), the rupture produces a relatively large detached pulse and oscillating slip rate further behind. As shown in Appendix, these oscillations of slip rate are well resolved numerically (Fig. 19), but their occurrence depends on the details of normal stress regularization and their wavelength depends on mesh size. This implies that the oscillations may be produced (at least partly) by the instability of a bimaterial fault configuration (COCHARD and RICE, 2000; RANJITH and RICE, 2001). Related discussion on the bimaterial instability can be found in Appendix, while here we mainly focus on evidence that the slip rate oscillations are modulated by fault zone waves.

Figure 12 presents detailed results of slip rates at different times, showing that the oscillations migrate

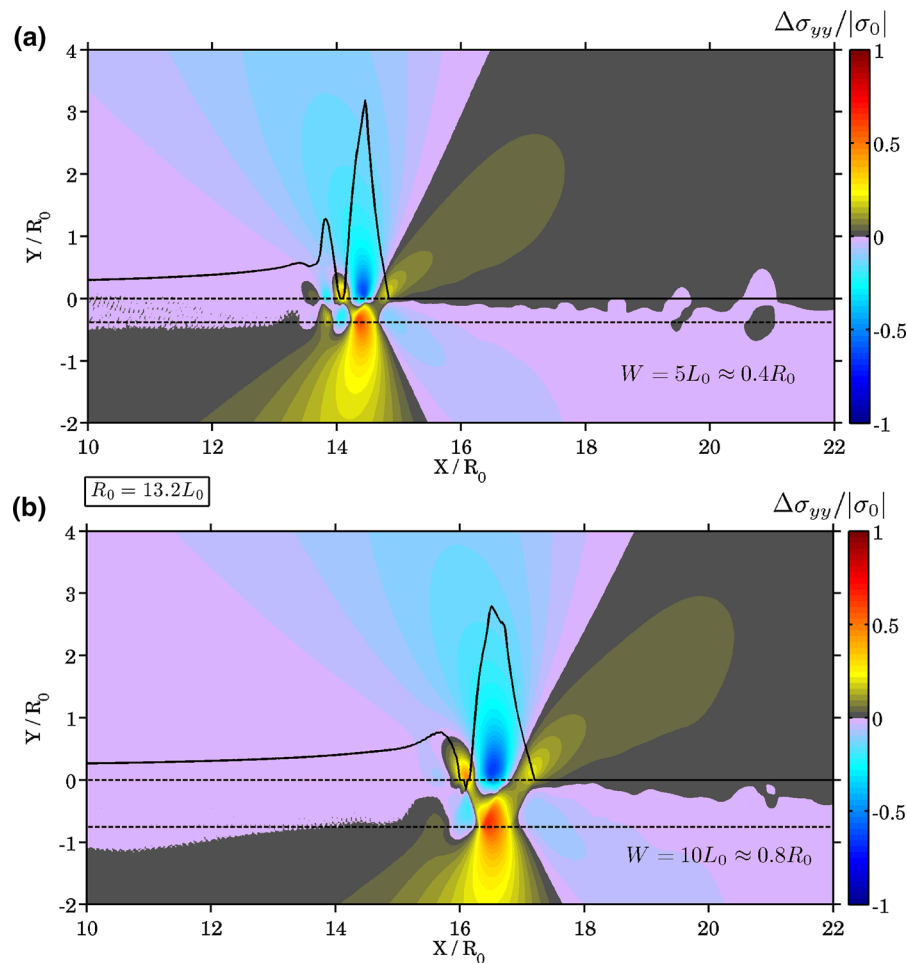


Figure 9

Snapshot distributions of $\Delta\sigma_{yy}$ for the case of Fig. 8a (a) and Fig. 8b (b) at times when a detached pulse front has just formed. The *solid black curve* shows the slip rate distribution for each plot. The *dashed black lines* indicate the boundaries of the pre-existing LVZ

towards the rupture propagation direction, with a somewhat expanding size. This is consistent with our expectation that they are triggered by a moving source (i.e., waves emitted from a propagating pulse front), although it is difficult to eliminate completely numerical artifacts that may also be triggered by a moving source or have a non-zero group velocity (see discussion in Appendix). The strong oscillations in slip rate and the long duration of the process imply that the anticipated internal wave reflections in the LVZ are more efficiently interacting with the frictional fault. To see this more explicitly, we plot the damage distribution and its off-fault variation (Fig. 13). The overall damage zone follows a similar pattern to that shown for the previous case in Fig. 6,

but the near-fault damage zone structures are quite different in the two cases. The current case has a more localized internal damage zone with very slowly growing width along strike and almost constant damage level. This is indicated by the dashed line in Fig. 13a and the overlap of different damage decay profiles close to the fault in Fig. 13b.

A comparison between the dominant wavelength of the oscillating slip rate in Fig. 12 and the damage zone structure in Fig. 13 suggests that the former is on the order of the width of the internal damage zone (having $\sim 30\%$ reduction in shear wave speed). Oscillation wavelengths and internal damage zone widths observed in several simulations are listed in Table 4 and are found to be roughly proportional.

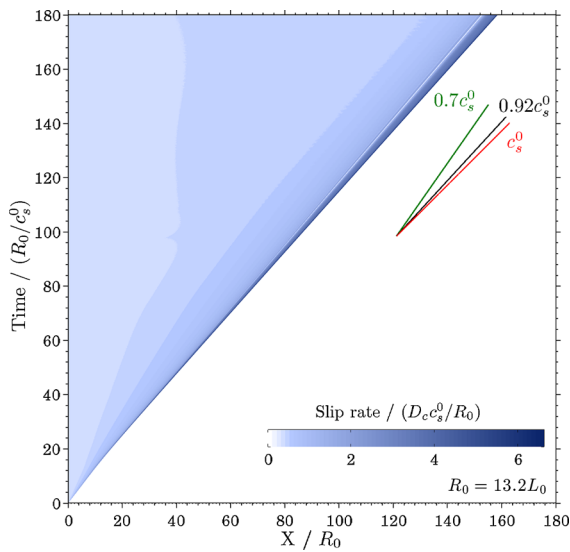


Figure 10

Spatio-temporal variation of slip rate for the case of Fig. 6. Various wave speeds of the intact or highly damaged rocks close to the fault (see Fig. 7a) are plotted for reference

Similar oscillations have been reported in models with pre-existing low velocity zone (e.g., HARRIS and DAY, 1997; BEN-ZION and HUANG, 2002; HUANG *et al.*, 2014). They were also observed in our elastic tests of rupture along the (bimaterial) boundary of very narrow pre-existing low velocity zones (not shown here). In addition, we find that the oscillation wavelength is also proportional to the mesh size (Fig. 19b). We conclude that while a bimaterial instability enables the emergence of slip rate oscillations far behind the rupture front, their monochromatic character is controlled by the finite thickness of the damage zone.

The current case develops slip rate oscillations during rupture propagation for the following reasons: (1) Its generated narrower damage zone near the fault enhances the development of trapped waves (BEN-ZION, 1998) because the number of reflections with significant amplitude increases with decreasing

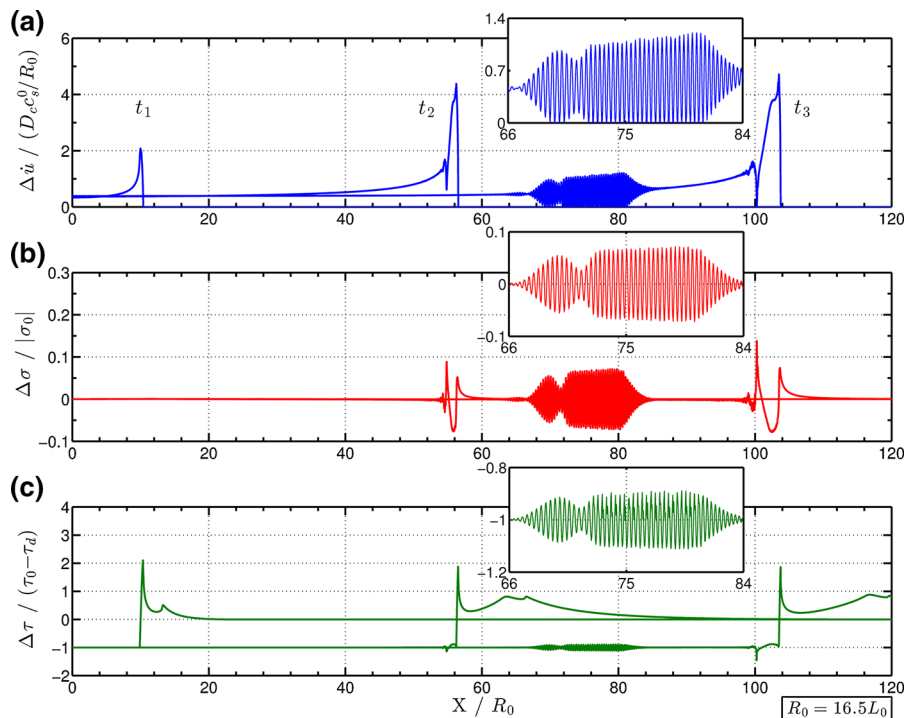


Figure 11

Similar to Fig. 5, but with slightly different model parameters: $f_d = 0.2$, $C_d = 0.8c_s^0/L_0 \approx 13.2c_s^0/R_0$, $q \approx 6.6c_s^0/R_0$, $C_g \approx 0.165c_s^0/(\mu_0 R_0)$, $C_v = 0$, $\beta = 0.1$. The chosen times highlight the moments when the propagating rupture behaves like a crack (t_1), with a partially detached pulse front (t_2) or a completely detached pulse front followed by a train of pulses (t_3)

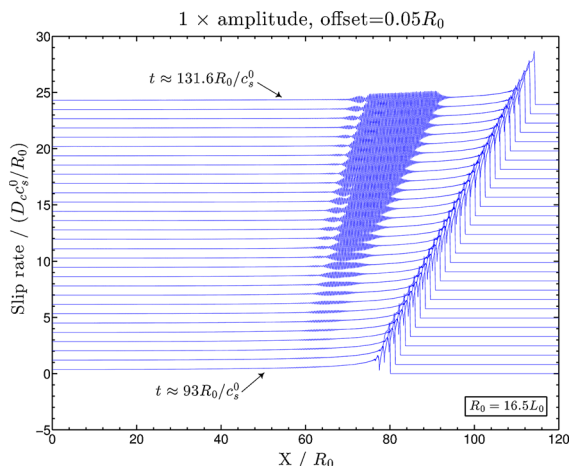


Figure 12

Spatial distribution of slip rate with persisting oscillations at different times for the case of Fig. 11

damage zone width if other factors remain about the same. (2) Its generated near-fault damage zone has approximately a constant width along strike, which

can construct trapped waves more coherently than with a spatially varying width (e.g., IGEL *et al.*, 1997; JAHNKE *et al.*, 2002). On the other hand, we notice that the slip rate oscillations appear only after the rupture has propagated over a certain distance range (Figs. 11, 12), and that they emerge at some distance behind the detached pulse front. These features may be explained by the fact that the number of oscillations of internal wave reflections and trapped waves increase with propagation distance (BEN-ZION, 1998), leading to larger cumulative interaction with the fault.

3.4. Modulation of the Rupture Front

From the previous results it is seen that radiated waves and their reflections within a LVZ can interact with the fault portion behind the rupture front. We also expect that the waves interact with the rupture front itself to produce oscillations of the rupture speed. Indeed, with a pre-existing constant-width

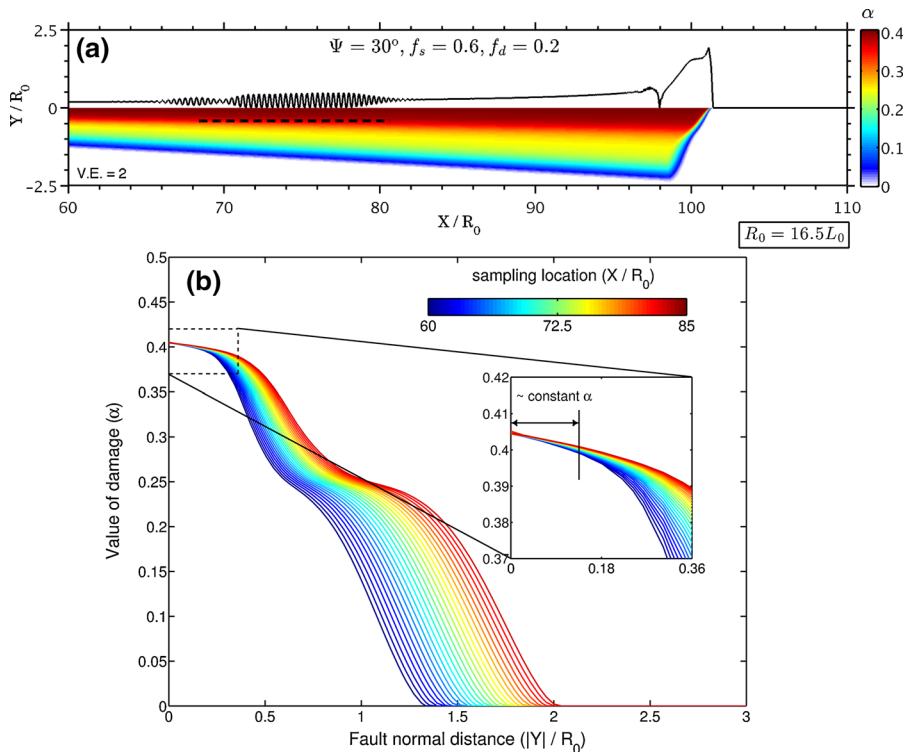


Figure 13

Snapshots distributions of (a) damage and (b) its off-fault variation for the case of Fig. 11. Slip rate at the same time is superimposed in (a). The color bar in (b) indicates how the sampling locations are mapped to different colors: from $X = 60R_0$ (blue) to $X = 85R_0$ (red)

Table 4

Relations between simulated oscillation wavelength of slip rate, width of internal damage zone (normalized by L_0), and maximum damage

Oscillation wavelength	Width	Maximum damage
0.7	0.2	0.4
1.5	0.4	0.4
1.8	0.5	0.3
3	0.6	0.3
10	2	0.4

LVZ, a simple geometric relation between the period of rupture speed oscillations and the rupture speed (in the subshear regime of the LVZ) and properties of the LVZ (width, wave speed) can be readily established (BEN-ZION and HUANG, 2002). Large rupture speed oscillations have been observed in numerical simulations with pre-existing LVZ (HUANG and AMPUERO, 2011; HUANG *et al.*, 2014). However, in the current study with evolving geometrical and material properties of the LVZ the results are more complex. The radiated waves in our case may initially propagate

with the speed of the intact material (there is no LVZ in some region around the rupture front), get later trapped inside an evolving LVZ and finally interact with the rupture front at its new position.

Since the backward-propagating waves and their reflections continuously produce healing signals behind the rupture front and modulate the stress drop, the stress concentration and energy release rate will be influenced by these fluctuations, leading to local acceleration or deceleration of the rupture speed. Figure 14 shows the evolution of smoothed rupture speed v_r (through 8-point averaging) and maximum slip rate v_{max} for the case leading to Fig. 5. As seen, beyond the location $X \sim 45R_0$, both v_r and v_{max} are locally modulated by quasi-periodic oscillations. The oscillations are well-resolved numerically and reflect a genuine physical outcome of the examined case. The coherence of the oscillating signals becomes stronger beyond $X \sim 92R_0$ (marked blue bar in Fig. 14), which corresponds to the location where a detached pulse front has just formed. These types of oscillations are observed for all the cases in our study where a detached pulse front is

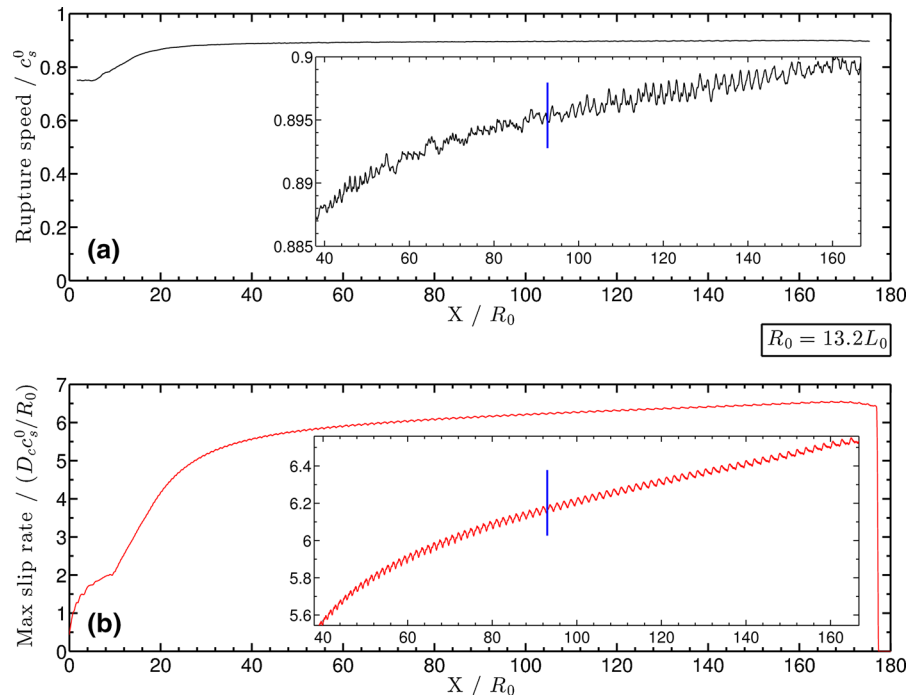


Figure 14

Spatial variations of (a) rupture speed and (b) maximum slip rate for the case of Fig. 5. The blue bar in the zoom-in view roughly indicates the location where a detached pulse front has formed for the first time

developed. It should be mentioned that the whole process is essentially non-linear because the perturbed rupture front determines the updated wave radiation and off-fault damage generation, which can influence the interference with the rupture front in a further step.

Additional simulation results indicate another scenario where the detached pulse front itself can become a train of pulses, which is usually associated with an extremely narrow and highly damaged zone close to the fault. However, in such a scenario we also find that high-intensity damage can localize, as shown also for plasticity (DUAN, 2008a), onto mesh edges close to the boundary of the generated (or pre-existing) narrow compliant zone in off-fault regions. This localization produces mesh-dependence for the simulation results, so the robustness of this scenario, and its implication for boundary Y-shears observed at the interfaces between fault gouge and country rocks (GU and WONG, 1994), should be more carefully investigated by our future work.

3.5. Effects on Near-Fault Ground Motion

So far we have focused on the interplay between the propagating rupture and radiated waves through the generated off-fault damage zone. Here, we consider in more detail the effects of the brittle damage zone on the near-fault ground motion.

Figure 15 shows the amplitude of particle velocity $|\dot{u}| = \sqrt{(\dot{u}_x)^2 + (\dot{u}_y)^2}$ for the case of Fig. 7. As seen, the pattern is almost symmetric across the fault ahead of the rupture front, because damage has not yet been

generated at those locations. In contrast, there is a strong asymmetry in the distribution of particle velocity right behind the rupture front, with higher amplitude over a wider off-fault distance range on the extensional side. This asymmetry can be well understood as due to the reduced seismic impedance and the possible multiple reflections of waves within the damage zone generated at that location. It is interesting to notice that the latter effect is directly connected to the wedge shape of the fresh damage zone near the rupture front (see Fig. 7a), which resembles the effect of a dipping fault and free surface on the amplified ground motion on the hanging wall (OGLESBY *et al.*, 1998; SHI and BRUNE, 2005).

Another asymmetry can be found in the ground motion further behind the rupture front. As discussed in Sect. 3.2, waves can be more coherently trapped inside a well-established damage zone, but will propagate away in a rather homogeneous medium. Therefore, receivers located on the side with damage generation are expected to record longer ground shaking with higher amplitude in the later part of seismograms than those on the other side. This is explicitly shown in fault-normal velocity seismograms in Fig. 16 for a linear array of receivers that is symmetrically distributed across the fault at $X = 106.1R_0$ (marked by a green line in Fig. 15). As seen, after the passage of the rupture front ($t > 126R_0/c_s^0$), receivers on the extensional side (red and below) continue to record oscillatory signals with low frequency and long duration. In contrast, receivers on the compressional side (blue and above) only record smooth motion that gradually reduces towards zero. This contrast is more pronounced in the fault-

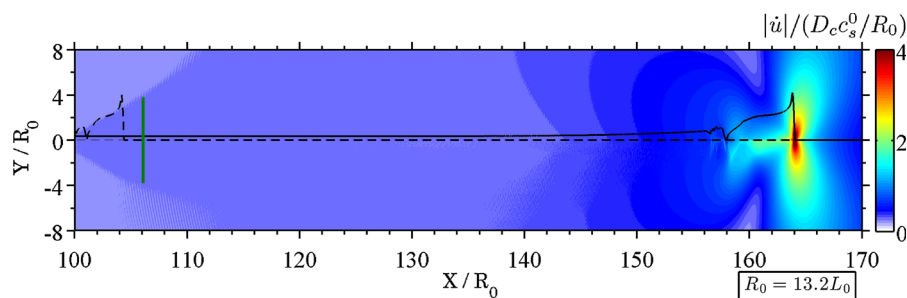


Figure 15

Snapshot distribution of amplitude of particle velocity at the same time as in Fig. 7. Two slip rate profiles are superimposed: the *solid one* corresponds to the same time as in Fig. 7, and the *dashed one* is associated with an earlier time when a completely detached pulse front has just formed. The *green line* indicates the location of receivers used in Fig. 16

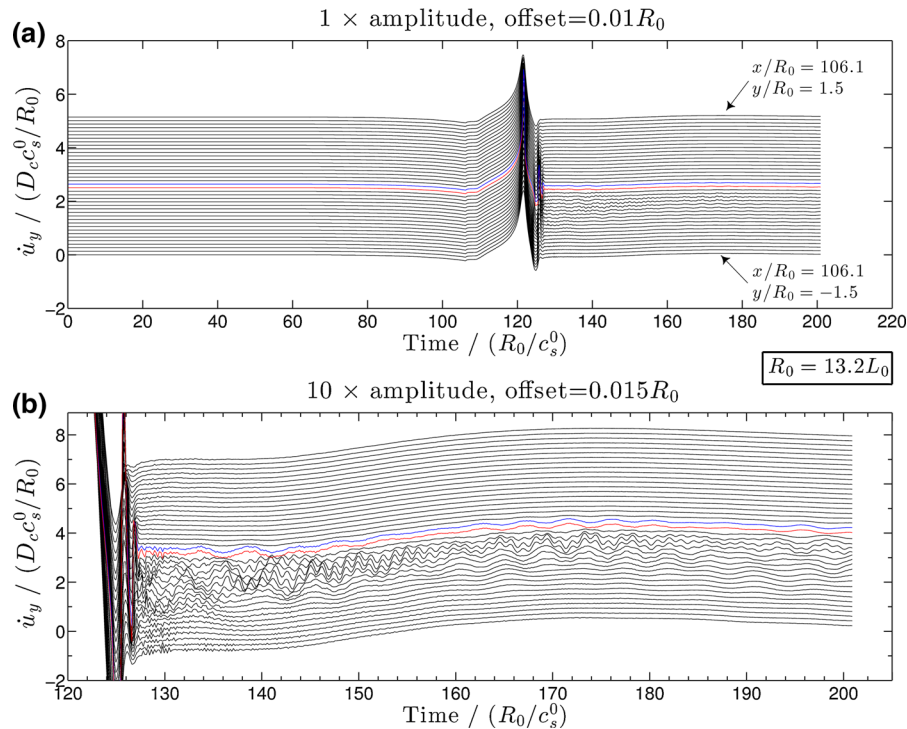


Figure 16

Velocity seismograms recorded by 40 receivers across the fault (green line in Fig. 15) in the fault-normal component (a) and its zoom-in view (b). Receivers are arranged from the extensional side (bottom, starting at $Y = -20L_0 \approx -1.5R_0$) to the compressional side (top, ending at $Y = 20L_0 \approx 1.5R_0$). The red and blue highlight the receivers nearest to the fault from the extensional and compressional side, respectively

normal component than in the fault-parallel component (not shown here), similar to the previous study with pre-existing LVZ surrounding the fault (DUAN, 2008a). Detailed investigation of seismograms on the extensional side also indicates that the first several receivers from the bottom are outside the effective waveguide, due to the lack of long-lived signal oscillations compared to those closer to the fault. This is confirmed by checking the mapped effective shear wave speed distribution where the internal LVZ (within the overall LVZ) has a thickness less than $1.5R_0$ around $X = 106.1R_0$.

4. Discussion

As mentioned in the text, there are some similarities between off-fault plasticity and brittle damage, including the equivalent onset criterion of yielding for intact rocks (Eq. 6) and the dependence of yielding zone properties on the background stress

and rupture mode (AMPUERO *et al.*, 2008; XU and BEN-ZION, 2013). However, there are also key differences between the two rheologies, with the most important being the fact that brittle damage changes the elastic moduli of the yielding material while plasticity does not. Another important difference is that in material with brittle damage the elastic slopes for stress–strain curves are different during loading and unloading, while they are the same for material with plastic yielding. Dynamic changes of elastic moduli and evolution of the effective moduli under loading and unloading conditions are well documented in laboratory experiments (e.g., ZOBACK and BYERLEE, 1975; GUPTA, 1973; LOCKNER *et al.*, 1977; WEINBERGER *et al.*, 1994; HAMIEL *et al.*, 2004) and have clear effects on various wave propagation phenomena (e.g., PENG and BEN-ZION, 2006; HAMIEL *et al.*, 2009; LYAKHOVSKY *et al.*, 2009; WU *et al.*, 2009). In the context of dynamic rupture problems, the changes of elastic moduli produced by brittle damage can produce strong interactions between various (reflected,

head, and trapped) waves and the rupture even at locations far behind the propagating front. Such strong interactions generally do not exist for plasticity, because the waves will simply propagate away unless other mechanisms are introduced. Therefore, several reported features in this study, such as detached pulse front and strong oscillations of slip rate, were not observed in previous corresponding studies (a uniform frictional fault without a pre-existing low velocity zone) employing off-fault plasticity.

Both brittle damage and plasticity are able to influence the tangent moduli that connect stress increments with total strain increments, which can be used to discuss instability leading to strain localization (LYAKHOVSKY *et al.*, 1997a, 2011; TEMPLETON and RICE, 2008). From this point of view, both rheologies can modify the stresses inside the yielding zones relative to the elastic levels, especially the on-fault normal stress when yielding occurs with an asymmetric pattern across the fault (Fig. 4 of this study; Figs. 4, 6 of ANDREWS, 2005). However, the detailed mechanism leading to such stress modifications can vary depending on the rheology. For Mohr–Coulomb plasticity, normal stress changes are mainly due to the asymmetric extent and/or orientation of stress relaxation across the fault (see, e.g. Figs. 6, 13, 14 in XU *et al.* (2012a) for illustration and example results from simulations with off-fault plasticity). For brittle damage used in this study, the changes of normal stress near the rupture front can be well explained by an anticipated bimaterial effect, in addition to other effects that may co-exist and are common to plasticity (see Sect. 3.1).

Various mechanisms have been proposed to produce pulse-like ruptures that can explain seismological observations of earthquakes with a short rise time (HEATON, 1990) and field observations on the lack of localized frictional heating near strike-slip faults (BRUNE *et al.*, 1969). These include rate-dependent friction (ZHENG and RICE, 1998), finite-width seismogenic zone (DAY, 1982), heterogeneities of fault strength or initial stress (BEROZA and MIKUMO, 1996), rupture on a bimaterial interface (ANDREWS and BEN-ZION, 1997), pre-existing symmetric or asymmetric LVZ (HARRIS and DAY, 1997; BEN-ZION and HUANG, 2002; HUANG and AMPUERO, 2011), and

generation of off-fault yielding by bimaterial ruptures (BEN-ZION and SHI, 2005; XU *et al.*, 2012b). In cases where multiple mechanisms co-exist, whether pulse-like ruptures can still be produced and their robustness depend strongly on competitive effects. In this study, we show that the spontaneous generation of off-fault brittle damage accounting for changing elastic moduli can also lead to the development of a pulse front. More specifically, we investigate the competition between a negative bimaterial effect (with a moderate-to-high Ψ value) and internal wave reflection by a finite-width LVZ (Sect. 3.2), and show that the latter can overcome the former under certain conditions. These conditions include a slowly growing or approximately constant-width damage zone, relatively large velocity contrast across the effective boundary of the damage-related LVZ, and relatively weak fault frictional strength behind the rupture front. Connecting the first condition to our model parameters, cases with $20^\circ \leq \Psi \leq 35^\circ$ while keeping other parameters (including the initial fault normal and shear stress components) the same as in Fig. 5 can successfully produce a detached pulse front within the range of $X < 152R_0$ (Fig. 17a).

Detailed investigation reveals the following features (Fig. 17b): (1) the critical rupture propagation distance producing a detached pulse front for the first time and the pulse width (see figure caption for definition) sampled at the same location increase with the Ψ value for $\Psi \geq 20^\circ$, which is associated with an increasing ratio of damage zone thickness to rupture propagation distance; (2) the pulse width with a fixed Ψ value increases with rupture propagation distance, which is associated with an increase of damage zone thickness. Similar correlation between pulse width and LVZ thickness can also be observed in elastic calculations with symmetric or asymmetric pre-existing LVZ (Fig. 8 of this study; results of HUANG and AMPUERO, 2011; HUANG *et al.*, 2014). This provides additional evidence for our expectation (Sect. 3.2) that the healing signal comes from the trapped waves inside the LVZ. The result summarized in Fig. 17 may also explain why YAMASHITA (2000) did not observe a detached pulse front in his numerical study by modeling off-fault tensile microcracks. In that case, the rupture either did not propagate over a long

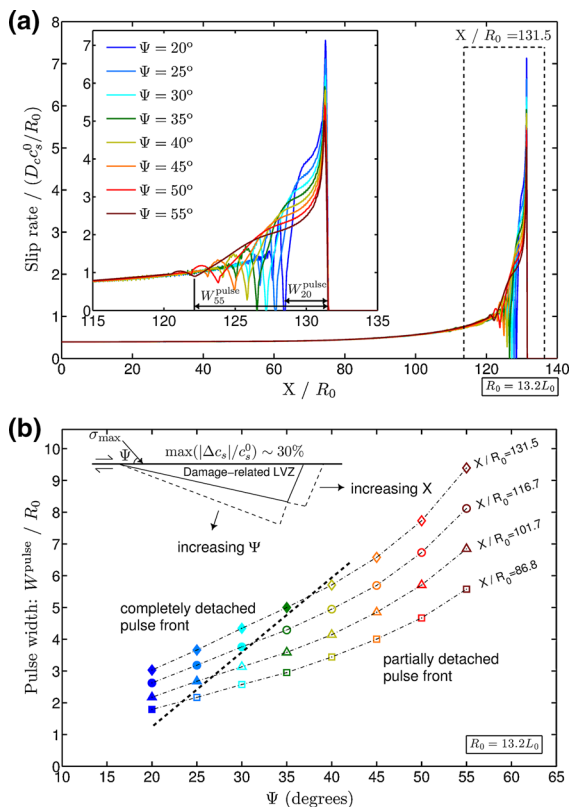


Figure 17

a Profiles of slip rate for cases with different Ψ values sampled at the same rupture front location ($X/R_0 = 131.5$). The *inset* shows the zoom-in view near the rupture front (indicated by the *dashed box*) where the width of a completely or partially detached pulse front can be defined. For cases with a partially detached pulse front, the effective tail of the pulse is defined as the first local trough in slip rate behind the rupture front. **b** Diagram showing the pulse width as a function of Ψ (indicated by *colors*) and sampling location (indicated by *marker shapes*). *Solid* and *open markers* represent completely and partially detached pulse fronts, respectively, and the *thick dashed line* roughly characterizes the boundary between the two. The *inset plot* in the *upper left corner* shows schematically the configuration of the generated LVZ with different Ψ values (for $\Psi \geq 20^\circ$) and rupture propagation distance

enough distance or the growing rate of LVZ thickness was too fast, although other factors such as material anisotropy and degree of velocity contrast may also be important for this topic.

In addition to a single, detached pulse front, our results also produce a rupture mode (Sect. 3.3) that has multiple pulses or show a tendency to develop into multiple pulses. This type of rupture mode has been seen in previous numerical studies under certain conditions. These include cases with pre-existing LVZ bounding the fault (HARRIS and DAY, 1997;

HUANG *et al.*, 2014), along with ruptures that are triggered by impact loadings (COKER *et al.*, 2005; SHI *et al.*, 2010), cases associated with highly energetic frictional nucleation procedure (SHI *et al.*, 2008), and cases with a relatively low background stress level coupled with a strong rate weakening friction (GABRIEL *et al.*, 2012). The mechanism leading to multiple rupture pulses in this work shares similarities with the mechanisms in previous studies with pre-existing LVZ, although there are also some differences. In HARRIS and DAY (1997) multiple pulses were observed with asymmetric LVZ primarily in the positive direction defined by a local bimaterial interface (Fig. 9a of their paper), while in HUANG *et al.* (2014) it was produced by a friction law with fast healing inside a symmetric, finite-width LVZ. Here, multiple pulses are observed with both dynamically generated as well as pre-existing LVZ (see Figs. 8, 11) on the extensional side, which corresponds to the negative direction of a bimaterial interface. The different LVZ configurations that produce multiple pulses suggest that internal wave reflections are a key generating mechanism that can dominate other effects over ranges of conditions.

The strong persisting oscillations of slip rate in Fig. 11 provide a possible mechanism for producing tremor-like signals in close proximity to the fault, although more work is needed to separate fully physical features from possibly coupled numerical artifacts. The mirror image of Fig. 11 from right to left represents a waveform recorded by a near-fault receiver, which is characterized (like tremor) by non-impulsive shape, long duration, and relatively low amplitude. The simulated results are most similar to harmonic volcanic tremors that are largely monochromatic and are typically explained in terms of fluid interaction with the boundary of a magma chamber (e.g., CHOUET, 2003). The process in this study is similar, but instead of fluid interactions, involves internally reflected waves with the boundary of a fault zone. More realistic simulations that incorporate pre-existing low velocity fault zone structure with variable width and velocity contrast, along with multiple operating sources [see, e.g. Figures 14–15 of BEN-ZION (1998)] are expected to generate more complex signals that may be relevant for volcanic and non-volcanic tremors. Variations of

frictional properties along the fault will lead to rupture acceleration and deceleration that may enhance the radiation of the generated signals to the far field. As mentioned in Sect. 3.3, the efficiency of the mechanism leading to strong persisting oscillations of slip rates increases for a LVZ with slowly varying narrow width, which may exist primarily at the bottom of or below the seismogenic zone. This implies that the mechanism for the discussed tremor-like near-fault signals should not operate at shallow depths, since fault damage zones typically display a flower-like structure toward the surface (BEN-ZION and SAMMIS, 2003; ROCKWELL and BEN-ZION, 2007; ALLAM and BEN-ZION, 2012).

The brittle damage model used in this study can provide, with additional simulations, multiple signals for interpretation of different elements of fault zone structures. As discussed in Section 7 of BEN-ZION (2008) and studied by LYAKHOVSKY *et al.* (2011) and LYAKHOVSKY and BEN-ZION (2014a, b), a brittle instability leading to dynamic rupture may correspond to a phase transition from a solid-like to a granular-like state of rocks. This corresponds physically to a transition from the fault damage zone where the rock volume still maintains cohesion to the slip zone filled with rock particles (gouge, cataclasite, etc.). The model suggests increasing rock damage density with proximity towards the fault core, followed by a possible saturation where rocks can no longer accommodate additional fracturing, but are crushed into finer grains, as has been documented by some field observations (e.g., MITCHELL and FAULKNER, 2009; ROCKWELL *et al.*, 2009; Wechsler *et al.*, 2011). This general feature of off-fault damage variation can be simulated with the adopted damage rheology during both dynamic ruptures (Fig. 6, Fig. 13) and under long-term, quasi-static loadings (BEN-ZION *et al.*, 1999; LYAKHOVSKY and BEN-ZION, 2009; FINZI *et al.*, 2009), with an explicit granular-related mechanism that can physically damp the damage growth (LYAKHOVSKY *et al.*, 2011). An important and challenging topic for a future study is multi-cycle simulations of fault zone evolution, accounting for damage accumulation and healing, as well as possible phase transitions in the states of rocks. This may be attempted in a follow up work.

Acknowledgments

We thank two anonymous referees and Editor Antonio Rovelli for useful comments. The study was supported by the National Science Foundation (Grants EAR-0944066, EAR-0944288 and EAR-0908903), the US–Israel Binational Science Foundation (Grant 2008248), and the Southern California Earthquake Center (based on NSF Cooperative Agreement EAR-0529922 and USGS Cooperative Agreement 07HQAC0026).

Appendix : Numerical Tests on the Robustness of Slip Rate Features

To assess the validity of results with oscillating fields, we conduct numerical tests on the robustness of the detached pulse front and slip rate oscillations. Two different mesh sizes are used, with possible modification of fault normal stress regularization, to test the accuracy and stability of the resulting ruptures.

Figure 18 shows simulated profiles of slip rate at two different times for the case of Fig. 5, with two different mesh sizes. In both examples, the process zone size, defined as the distance from the onset of slip to the peak slip velocity, is resolved by about six nodes with the coarser mesh. Although there are slight differences in the onset of slip and local peak or trough values, the overall profiles match well, including the resolution of the healing signal behind the rupture front. Figure 19 shows test results for the case of Fig. 11 where we vary parameters of the normal stress regularization and the mesh size. We use an estimated time scale $t^* = \frac{\delta_c}{V^* + |V|}$ to quantify the effect of normal stress regularization, with extremely small and relatively large t^* values corresponding, respectively, to almost instantaneous and slightly delayed response of frictional strength to fault normal stress changes. Nominal t^* values are evaluated here with $V = 2V^*$. As seen, the resolved pulse front profiles with the three tested t^* values overlap well with each other (Fig. 19a). This is because these t^* values are small compared to the time scale of the frictional weakening process, which is of the order of the travel time of a shear wave through R_0 . In

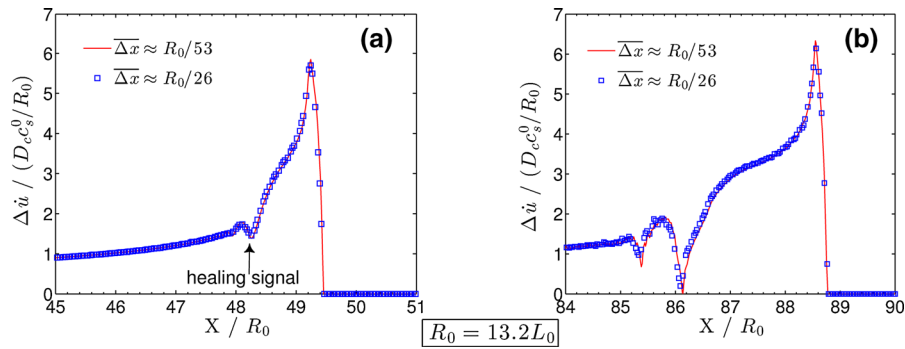


Figure 18

Numerical tests on the resolutions of slip rate (see Fig. 5 for reference) with two different mesh sizes. **a** At an earlier time with a weak healing signal, and **b** at a later time with sufficiently strong healing to produce a completely detached pulse front

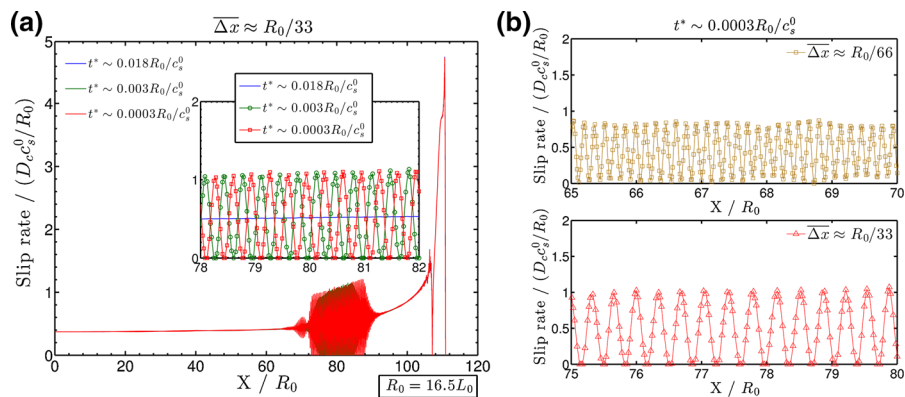


Figure 19

Numerical tests on the stability and resolution of oscillating slip rate (see Fig. 11 for reference) with **(a)** various model parameters for the normal stress regularization and **(b)** different mesh sizes. See the text for the definition of t^*

addition, off-fault energy dissipation due to damage and the plasticity-related stress relaxation near the rupture front can help stabilize the slip rate (BEN-ZION and SHI, 2005), so that the details of the normal stress regularization become less important at that location. We thus conclude that the detached pulse front is a robust feature.

However, at locations further behind the rupture front where the generated damage is frozen, the assumed t^* value can significantly affect the rupture behavior (inset of Fig. 19a). The two cases with small t^* values (green and red) preserve slip rate oscillations with about the same wavelength, although different phases (see the inset plot), while the case with largest t^* (blue) produces a smooth slip rate profile without significant oscillations. A further investigation with the smallest t^* value shows that the slip rate oscillations depend on mesh size: the

oscillation wavelength decreases with refining the mesh size (Fig. 19b).

Based on above results, one may argue that the resulting slip rate oscillations with small t^* values are produced by the numerical instability known for bi-material problems (COCHARD and RICE, 2000; RANJITH and RICE, 2001): the fault portion far behind the rupture front is undergoing quasi-steady sliding with a bi-material configuration under a constant friction ($f = f_d$), and is constantly perturbed by the trapped waves that are initially emitted from the detached pulse front. However, in contrast to typical artifacts related to the bi-material effect, the slip rate oscillations do not diverge with time, perhaps partly due to the incorporated visco-elastic damping near the fault. The oscillation amplitude appears to saturate at a value controlled by the background slip velocity. Moreover, the slip rate oscillations are quite

monochromatic, suggesting a process characterized by a dominant length scale such as the thickness of the internal damage zone waveguide (see Fig. 13). Section 3.3 in the main text gives some physical perspectives on the possible origin of such slip rate oscillations, as a comparison to the case in Fig. 5 without oscillations. We conclude that the observed slip rate oscillations are likely induced by a physical process involving interaction with trapped waves, superposed with a numerical instability due to the bimaterial fault configuration. Current understanding of fault friction based on laboratory experiments (e.g., KILGORE *et al.*, 2012) suggests a delayed frictional strength response to a sudden step-like normal stress change. Additional future work involving a bimaterial fault loaded by an oscillating normal stress should be done to fully understand the results associated with the simulated slip rate oscillations.

REFERENCES

- ALLAM, A.A., and BEN-ZION, Y., (2012), *Seismic velocity structures in the Southern California plate-boundary environment from double-difference tomography*, *Geophys. J. Int.*, *190*, 1181–1196, doi:10.1111/j.1365-246X.2012.05544.x.
- AMPUERO, J.-P., (2002), Etude physique et numérique de la nucléation des séismes. Ph. D. thesis, Université Paris 7, Denis Diderot, Paris.
- AMPUERO, J.-P., SEM2DPAK-2.3.8, (2012), Available at: <http://sourceforge.net/projects/sem2d/>.
- AMPUERO, J.-P., and BEN-ZION, Y., (2008), *Cracks, pulses and macroscopic asymmetry of dynamic rupture on a bimaterial interface with velocity-weakening friction*, *Geophys. J. Int.*, *173*, 674–692.
- AMPUERO, J.-P., BEN-ZION, Y., and LYAKHOVSKY, V., (2008), *Interaction between dynamic rupture and off-fault damage*, *Seism. Res. Lett.*, *79*(2), 295.
- ANDREWS, D.J., (1976), *Rupture velocity of plane strain shear cracks*, *J. Geophys. Res.*, *81*, 5679–5687.
- ANDREWS, D.J., (2005), *Rupture dynamics with energy loss outside the slip zone*, *J. Geophys. Res.*, *110*, B01307, doi:10.1029/2004JB003191.
- ANDREWS, D.J., HANKS, T.C., and WHITNEY, J.W., (2007), *Physical limits on ground motion at Yucca Mountain*, *Bull. Seism. Soc. Am.* *97*, 1771–1792, doi:10.1785/0120070014.
- ANDREWS, D.J., and BEN-ZION, Y., (1997), *Wrinkle-like slip pulse on a fault between different materials*, *J. Geophys. Res.*, *102*, 553–571.
- AVALLONE, A., ROVELLI, A., DI GIULIO, G., IMPROTA, L., BEN-ZION, Y., MILANA, G., and CARA, F., (2014), *Wave-guide effects in very high rate GPS record of the 6 April 2009, Mw 6.1 L'Aquila, central Italy earthquake*, *J. Geophys. Res.*, *119*, 490–501, doi:10.1002/2013JB010475.
- BEN-ZION, Y., (1989), *The response of two joined quarter-space to SH line sources located at the material discontinuity interface*, *Geophys. J. Int.*, *98*, 213–222.
- BEN-ZION, Y., (1990), *The response of two half-spaces to point dislocations at the material interface*, *Geophys. J. Int.*, *101*, 507–528.
- BEN-ZION, Y., (1998), *Properties of seismic fault zone waves and their utility for imaging low velocity structures*, *J. Geophys. Res.*, *103*, 12567–12585.
- BEN-ZION, Y., (2001), *Dynamic ruptures in recent models of earthquake faults*, *J. Mech. Phys. Solids*, *49*, 2209–2244.
- BEN-ZION, Y., (2008), *Collective behavior of earthquakes and faults: Continuum-discrete transitions, progressive evolutionary changes, and different dynamic regimes*, *Rev. Geophys.*, *46*, RG4006, doi:10.1029/2008RG000260.
- BEN-ZION, Y., and AKI, K., (1990), *Seismic radiation from an SH line source in a laterally heterogeneous planar fault zone*, *Bull. Seism. Soc. Amer.*, *80*, 971–994.
- BEN-ZION, Y., and AMPUERO, J.-P., (2009), *Seismic radiation from regions sustaining material damage*, *Geophys. J. Int.*, *178*, 1351–1356, doi:10.1111/j.1365-246X.2009.04285.x.
- BEN-ZION, Y., and ANDREWS, D.J., (1998), *Properties and implications of dynamic rupture along a material interface*, *Bull. Seism. Soc. Amer.*, *88*, 1085–1094.
- BEN-ZION, Y., DAHMEN, K., LYAKHOVSKY, V., ERTAS, D., and AGNON, A., (1999), *Self-driven mode switching of earthquake activity on a fault system*, *Earth Planet. Sci. Lett.*, *172*/1–2, 11–21.
- BEN-ZION, Y., and HUANG, Y., (2002), *Dynamic rupture on an interface between a compliant fault zone layer and a stiffer surrounding solid*, *J. Geophys. Res.*, *107*(B2), 2042, doi:10.1029/2001JB000254.
- BEN-ZION, Y., and LYAKHOVSKY, V., (2002), *Accelerated seismic release and related aspects of seismicity patterns on earthquake faults*, *Pure Appl. Geophys.*, *159*, 2385–2412.
- BEN-ZION, Y., and LYAKHOVSKY, V., (2006), *Analysis of aftershocks in a lithospheric model with seismogenic zone governed by damage rheology*, *Geophys. J. Int.*, *165*, 197–210, doi:10.1111/j.1365-246X.2006.02878.x.
- BEN-ZION, Y., and SAMMIS, C.G., (2003), *Characterization of Fault Zones*, *Pure Appl. Geophys.*, *160*, 677–715.
- BEN-ZION, Y., and SHI, Z., (2005), *Dynamic rupture on a material interface with spontaneous generation of plastic strain in the bulk*, *Earth Planet. Sci. Lett.*, *236*, 486–496, doi:10.1016/j.epsl.2005.03.025.
- BEROZA, G.C., and MIKUMO, T., (1996), *Short time duration in dynamic rupture in the presence of heterogeneous fault properties*, *J. Geophys. Res.*, *101*(B10), 22,449–22,460, doi:10.1029/96JB02291.
- BRUNE, J.N., HENYEV, T.L., and ROY, R. F., (1969), *Heat flow, stress and rate of slip along the San Andreas Fault, California*, *J. Geophys. Res.*, *74*, 3821–3827, doi:10.1029/JB074i015p03821.
- BUDIANSKY, B., and O'CONNELL, R.J., (1976), *Elastic moduli of a cracked solid*, *Int. J. Solids Struct.*, *12*, 81–97.
- BURRIDGE, R., (1973), *Admissible speeds for plane-strain self-similar shear cracks with friction but lacking cohesion*, *Geophys. J. R. Astr. Soc.*, *35*, 439–455.
- CHOUET, B., (2003), *Volcano Seismology*, *Pure Appl. Geophys.*, *160*, 739–788.
- COCHARD, A., and RICE, J.R., (2000), *Fault rupture between dissimilar materials: Ill-posedness, regularization, and slip pulse response*, *J. Geophys. Res.*, *105*, 25,891–25,907.

- COCKER, D., LYKOTRAFITIS, G., NEEDLEMAN, A., and ROSAKIS, A.J., (2005), *Frictional sliding modes along an interface between identical elastic plates subject to shear impact loading*, *J. Mech. Phys. Solids*, 53, 884–992.
- DAS, S., and AKI, K., (1977), *A numerical study of two-dimensional spontaneous rupture propagation*, *Geophys. J. R. Astr. Soc.*, 50(3), 643–668, doi:10.1111/j.1365-246X.1977.tb01339.x.
- DAY, S.M., (1982), *Three-dimensional finite difference simulation of fault dynamics: Rectangular faults with fixed rupture velocity*, *Bull. Seism. Soc. Am.*, 72, 705–727.
- DE DONTNEY, N., TEMPLETON-BARRETT, E.L., RICE, J.R., and DMOWSKA, R., (2011), *Influence of plastic deformation on bi-material fault rupture directivity*, *J. Geophys. Res.*, 116, B10312, doi:10.1029/2011JB008417.
- DI TORO, G., HAN, R., HIROSE, T., DE PAOLA, N., NIELSEN, S., MIZOGUCHI, K., FERRI, F., COCCO, M., and SHIMAMOTO, T., (2011), *Fault lubrication during earthquakes*, *Nature*, 471(7339), 494, doi:10.1038/nature09838.
- DUAN, B., (2008a), *Effects of low-velocity fault zones on dynamic ruptures with nonelastic off-fault response*, *Geophys. Res. Lett.*, 35, L04307, doi:10.1029/2008GL033171.
- DUAN, B., (2008b), *Asymmetric off-fault damage generated by bilateral ruptures along a bimaterial interface*, *Geophys. Res. Lett.*, 35, L14306, doi:10.1029/2008GL034797.
- DUAN, B., and DAY, S.M., (2008), *Inelastic strain distribution and seismic radiation from rupture of a fault kink*, *J. Geophys. Res.*, 113, B12311, doi:10.1029/2008JB005847.
- DUNHAM, E.M., BELANGER, D., CONG, L., and KOZDON, J.E., (2011), *Earthquake ruptures with strongly rate-weakening friction and off-fault plasticity. 1: Planar faults*, *Bull. Seism. Soc. Am.*, 101(5), 2296–2307.
- FESTA, G., and VILLOTTE, J.-P., (2006), *Influence of the rupture initiation on the intersonic transition: Crack-like versus pulse-like modes*, *Geophys. Res. Lett.*, 33, L15320.
- FINZI, Y., HEARN, E.H., BEN-ZION, Y., and LYAKHOVSKY, V., (2009), *Structural properties and deformation patterns of evolving strike-slip faults: numerical simulations incorporating damage rheology*, *Pure Appl. Geophys.*, 166, 1537–1573, doi:10.1007/s00024-009-0522-1.
- FROMENT B., CAMPILLO, M., CHEN, J.H., and LIU, Q.Y., (2013), *Deformation at depth associated with the 12 May 2008 MW 7.9 Wenchuan earthquake from seismic ambient noise monitoring*, *Geophys. Res. Lett.*, 40, doi:10.1029/2012GL053995.
- GABRIEL, A.A., AMPUERO, J.-P., DALGUER, L.A., and MAI, P.M., (2012), *The transition of dynamic rupture styles in elastic media under velocity-weakening friction*, *J. Geophys. Res.*, 117, B09311, doi:10.1029/2012JB009468.
- GABRIEL, A.A., AMPUERO, J.-P., DALGUER, L.A., and MAI, P.M., (2013), *Source properties of dynamic rupture pulses with off-fault plasticity*, *J. Geophys. Res.*, 118, doi:10.1002/jgrb.50213.
- GU, Y.J., and WONG, T.-F., (1994), *Development of shear localization in simulated quartz gouge: effect of cumulative slip and gouge particle size*, *Pure Appl. Geophys.*, 143(1-3), 387–423.
- GUPTA, I., (1973), *Seismic velocities in rock subjected to axial loading up to shear fracture*, *J. Geophys. Res.*, 78(29), 6936–6942.
- HAMIEL, Y., LIU, Y., LYAKHOVSKY, V., BEN-ZION, Y., and LOCKNER, D., (2004), *A viscoelastic damage model with applications to stable and unstable fracturing*, *Geophys. J. Int.*, 159, 1155–1165.
- HAMIEL, Y., LYAKHOVSKY, V., STANCHITS, S., DRESEN, G., and BEN-ZION, Y., (2009), *Brittle deformation and damage-induced seismic wave anisotropy in rocks*, *Geophys. J. Int.*, 178, 901–909, doi:10.1111/j.1365-246X.2009.04200.x.
- HARRIS, R.A., and DAY, S.M., (1997), *Effects of a low-velocity zone on a dynamic rupture*, *Bull. Seism. Soc. Am.*, 87, 1267–1280.
- HEATON, T.H., (1990), *Evidence for and implications of self-healing pulses of slip in earthquake rupture*, *Phys. Earth planet. Inter.*, 64, 1–20.
- HUANG, Y., and AMPUERO, J.-P., (2011), *Pulse-like ruptures induced by low-velocity fault zones*, *J. Geophys. Res.*, 116, B12307, doi:10.1029/2011JB008684.
- HUANG, Y., AMPUERO, J.-P., and HELMBERGER, D.V., (2014), *Earthquake ruptures modulated by waves in damaged fault zones*, *J. Geophys. Res.*, 119, doi:10.1002/2013JB010724.
- IDA, Y., (1972), *Cohesive force across tip of a longitudinal-shear crack and Griffith's specific surface-energy*, *J. Geophys. Res.*, 77, 3796–3805.
- IGEL, H., BEN-ZION, Y., and LEARY, P., (1997), *Simulation of SH and P-SV wave propagation in fault zones*, *Geophys. J. Int.*, 128, 533–546.
- JAHNKE, G., IGEL, H., and BEN-ZION, Y., (2002), *Three-dimensional calculations of fault-zone-guided waves in various irregular structures*, *Geophys. J. Int.*, 151, 416–426.
- Kaneko, Y., and Fialko, Y., (2011), *Shallow slip deficit due to large strike-slip earthquakes in dynamic rupture simulations with elasto-plastic off-fault response*, *Geophys. J. Int.*, 186, 1389–1403, doi:10.1111/j.1365-246X.2011.05117.x.
- KILGORE, B., LOZOS, J., BEELER, N., and OGLESBY, D., (2012), *Laboratory observations of fault strength in response to changes in normal stress*, *J. Appl. Mech.*, 79, 031007, doi:10.1115/1.4005883.
- LOCKNER, D., WALSH, J., and BYERLEE, J., (1977), *Changes in seismic velocity and attenuation during deformation of granite*, *J. Geophys. Res.*, 82, 5374–5378.
- LOCKNER, D.A., and BYERLEE, J.D., (1980), *Development of fracture planes during creep in granite: in 2nd Conference on Acoustic Emission/Microseismic activity in Geological Structure and materials*, 1–25, Trans Tech., Clausthal-Zellerfeld, Germany.
- LOCKNER, D.A., and BEELER, N.M., (2002), *Rock failure and earthquakes*, in *International Handbook of Earthquake and Engineering Seismology*, pp. 505–537, eds Lee, W.H.K., Kanamori, H., Jennings, P.C. & Kisslinger, C., Academic Press, Amsterdam.
- LYAKHOVSKY, V., BEN-ZION, Y., and AGNON, A., (1997a), *Distributed damage, faulting, and friction*, *J. Geophys. Res.*, 102(B12), 27,635–27,649, doi:10.1029/97JB01896.
- LYAKHOVSKY, V., RECHES, Z., WEINBERGER, R., and SCOTT, T.E., (1997b), *Non-linear elastic behavior of damaged rocks*, *Geophys. J. Int.*, 130, 157–166.
- LYAKHOVSKY, V., and BEN-ZION, Y., (2008), *Scaling relations of earthquakes and aseismic deformation in a damage rheology model*, *Geophys. J. Int.*, 172, 651–662, doi:10.1111/j.1365-246X.2007.03652.x.
- LYAKHOVSKY, V., and BEN-ZION, Y., (2009), *Evolving geometrical and material properties of fault zones in a damage rheology model*, *Geochem. Geophys. Geosyst.*, 10, Q11011, doi:10.1029/2009GC002543.
- LYAKHOVSKY, V., and BEN-ZION, Y., (2014a), *Damage-breakage rheology model and solid-granular transition near brittle instability*, *J. Mech. Phys. Solids.*, 64, 184–197, doi:10.1016/j.jmps.2013.11.007.
- LYAKHOVSKY, V., and BEN-ZION, Y. (2014b), *A continuum damage-breakage faulting model accounting for solid-granular transitions*, *Pure Appl. Geophys.*, 171, doi:10.1007/s00024-014-0845-4.

- LYAKHOVSKY, V., HAMIEL, Y., AMPUERO, J.-P., and BEN-ZION, Y., (2009), *Non-linear damage rheology and wave resonance in rocks*, *Geophys. J. Int.*, *178*, 910–920, doi:[10.1111/j.1365-246X.2009.04205.x](https://doi.org/10.1111/j.1365-246X.2009.04205.x).
- LYAKHOVSKY, V., HAMIEL, Y., and BEN-ZION, Y., (2011), *A non-local visco-elastic damage model and dynamic fracturing*, *J. Mech. Phys. Solids*, *59*, 1752–1776, doi:[10.1016/j.jmps.2011.05.016](https://doi.org/10.1016/j.jmps.2011.05.016).
- MA, S., and ANDREWS, D.J., (2010), *Inelastic off-fault response and three-dimensional dynamics of earthquake rupture on a strike-slip fault*, *J. Geophys. Res.*, *115*, B04304, doi:[10.1029/2009JB006382](https://doi.org/10.1029/2009JB006382).
- MITCHELL, T.M., and FAULKNER, D.R., (2009), *The nature and origin of off-fault damage surrounding strike-slip fault zones with a wide range of the displacements: A field study from the Atacama fault system, northern Chile*, *J. Struct. Geol.*, *31*, 802–816.
- OGLESBY, D.D., ARCHULETA, R., and NIELSEN, S.B., (1998), *Earthquakes on dipping faults: The effects of broken symmetry*, *Science*, *280*, 1055–1059, doi:[10.1126/science.280.5366.1055](https://doi.org/10.1126/science.280.5366.1055).
- PALMER, A.C., and RICE, J.R., (1973), *Growth of slip surfaces in progressive failure of over-consolidated clay*, *Proc. R. Soc. London, Ser. A.*, *332*, 527–548.
- PENG, Z., and BEN-ZION, Y., (2006), *Temporal changes of shallow seismic velocity around the Karadere-Düzce branch of the North Anatolian Fault and strong ground motion*, *Pure appl. Geophys.*, *163*, 567–600, doi:[10.1007/s00024-005-0034-6](https://doi.org/10.1007/s00024-005-0034-6).
- RANJITH, K., and RICE, J.R., (2001), *Slip dynamics at an interface between dissimilar materials*, *J. Mech. Phys. Solids*, *49*, 341–361.
- RICE, J.R., (1980), *The mechanics of earthquake rupture*: in *Physics of Earth's Interior*, eds Dzieswonski A.M. & Boschi, E., *Proc. Int. Sch. Phys. Enrico Fermi*, *78*, 555–649.
- ROCKWELL, T.K., and BEN-ZION Y., (2007), *High localization of primary slip zones in large earthquakes from paleoseismic trenches, Observations and implications for earthquake physics*, *J. Geophys. Res.*, *112*, B10304, doi:[10.1029/2006JB004764](https://doi.org/10.1029/2006JB004764).
- ROCKWELL, T., SISK, M., GIRTY, G., DOR, O., WECHSLER, N., and BEN-ZION, Y., (2009), *Chemical and Physical Characteristics of Pulverized Tejon Lookout Granite Adjacent to the San Andreas and Garlock Faults: Implications for Earthquake Physics*, *Pure Appl. Geophys.*, *166*, 1725–1746, doi:[10.1007/s00024-009-0514-1](https://doi.org/10.1007/s00024-009-0514-1).
- RUBIN, A.M., and AMPUERO, J.-P., (2007), *Aftershock asymmetry on a bimaterial interface*, *J. Geophys. Res.*, *112*, B05307, doi:[10.1029/2006JB004337](https://doi.org/10.1029/2006JB004337).
- SHI, Z., and BEN-ZION, Y., (2006), *Dynamic rupture on a bimaterial interface governed by slip-weakening friction*, *Geophys. J. Int.*, *165*, 469–484.
- SHI, Z., BEN-ZION, Y., and NEEDLEMAN, A., (2008), *Properties of dynamic rupture and energy partition in a two-dimensional elastic solid with a frictional interface*, *J. Mech. Phys. Solids*, *56*, 5–24, doi:[10.1016/j.jmps.2007.04.006](https://doi.org/10.1016/j.jmps.2007.04.006).
- SHI, Z., NEEDLEMAN, A., and BEN-ZION, Y., (2010), *Slip modes and partitioning of energy during dynamic frictional sliding between identical elastic viscoplastic solids*, *Int. J. Fract.*, *162*, 51–67, doi:[10.1007/s10704-009-9388-6/](https://doi.org/10.1007/s10704-009-9388-6/).
- SHI, B., and BRUNE, J.N., (2005), *Characteristics of near-fault ground motions by dynamic thrust faulting: two-dimensional lattice particle approaches*, *Bull. Seism. Soc. Am.*, *95*(6), 2525–2533, doi:[10.1785/0120040227](https://doi.org/10.1785/0120040227).
- SPUDICH, P., and OLSEN, K.B., (2001), *Fault zone amplified waves as a possible seismic hazard along the Calaveras fault in central California*, *Geophys. Res. Lett.*, *28*, 2533–2536.
- STANCHITS, S., VINCIGUERRA, S., and DRESEN, G., (2006), *Ultrasonic velocities, acoustic emission characteristics and crack damage of basalt and granite*, *Pure Appl. Geophys.*, *163*, 975–993, doi:[10.1007/s00024-006-0059-5](https://doi.org/10.1007/s00024-006-0059-5).
- TEMPLETON, E.L., and RICE, J.R., (2008), *Off-fault plasticity and earthquake rupture dynamics: 1. Dry materials or neglect of fluid pressure changes*, *J. Geophys. Res.*, *113*, B09306, doi:[10.1029/2007JB005529](https://doi.org/10.1029/2007JB005529).
- WECHSLER, N., ALLEN, E.E., ROCKWELL, T.K., GIRTY, G., CHESTER, J.S., and BEN-ZION, Y., (2011), *Characterization of Pulverized Granitoids in a Shallow Core along the San Andreas Fault, Little Rock, CA*, *Geophys. J. Int.*, *186*, 401–417, doi:[10.1111/j.1365-246X.2011.05059.x](https://doi.org/10.1111/j.1365-246X.2011.05059.x).
- WEERTMAN, J., (1980), *Unstable slippage across a fault that separates elastic media of different elastic constants*, *J. Geophys. Res.*, *85*(B3), 1455–1461, doi:[10.1029/JB085iB03p01455](https://doi.org/10.1029/JB085iB03p01455).
- WEERTMAN, J., (2002) *Subsonic type earthquake dislocation moving at approximately $\sqrt{2}$ shear wave velocity on interface between half spaces of slightly different elastic constants*, *Geophys. Res. Lett.*, *29*(10), doi:[10.1029/2001GL013916](https://doi.org/10.1029/2001GL013916).
- WEINBERGER, R., RECHES, Z., SCOTT, T.S., and EIDELMAN, A., (1994), *Tensile properties of rocks in four-point beam tests under confining pressure*, pp. 435–442, in: *Proceedings First North American Rock Mechanics Symposium*, Austin, Texas.
- WU, C., PENG, Z., and BEN-ZION, Y., (2009), *Non-linearity and temporal changes of fault zone site response associated with strong ground motion*, *Geophys. J. Int.*, *176*, 265–278, doi:[10.1111/j.1365-246X.2008.04005.x](https://doi.org/10.1111/j.1365-246X.2008.04005.x).
- XU, S., BEN-ZION, Y., and AMPUERO, J.-P., (2012a), *Properties of inelastic yielding zones generated by in-plane dynamic ruptures: 1. Model description and basic results*, *Geophys. J. Int.*, *191*, 1325–1342, doi:[10.1111/j.1365-246X.2012.05679.x](https://doi.org/10.1111/j.1365-246X.2012.05679.x).
- XU, S., BEN-ZION, Y., and AMPUERO, J.-P., (2012b), *Properties of inelastic yielding zones generated by in-plane dynamic ruptures: 2. Detailed parameter-space study*, *Geophys. J. Int.*, *191*, 1343–1360, doi:[10.1111/j.1365-246X.2012.05685.x](https://doi.org/10.1111/j.1365-246X.2012.05685.x).
- XU, S., and BEN-ZION, Y., (2013), *Numerical and theoretical analyses of in-plane dynamic rupture on a frictional interface and off-fault yielding patterns at different scales*, *Geophys. J. Int.*, *193*, 304–320, doi:[10.1093/gji/ggs105](https://doi.org/10.1093/gji/ggs105).
- YAMASHITA, T., (2000), *Generation of microcracks by dynamic shear rupture and its effects on rupture growth and elastic wave radiation*, *Geophys. J. Int.*, *143*, 395–406.
- ZHENG, G., and RICE, J.R., (1998), *Conditions under which velocity-weakening friction allows a self-healing versus a crack-like mode of rupture*, *Bull. Seism. Soc. Am.*, *88*, 1466–1483.
- ZOBACK, M.D., and BYERLEE, J.D., (1975), *The effect of microcrack dilatancy on the permeability of Western granite*, *J. Geophys. Res.*, *80*, 752–755.